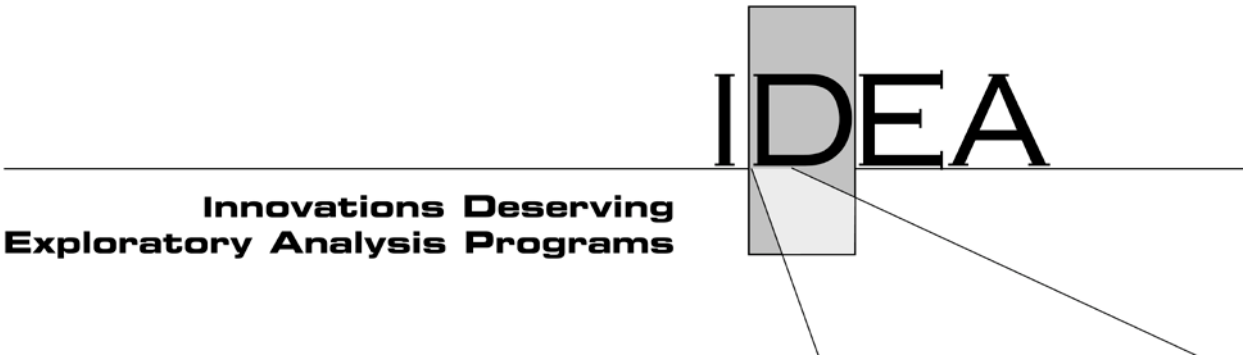


***Safety IDEA Program***

# Materials with Improved Absorption of Collision Forces for Railroad Cars

Final Report for
Safety IDEA Project 20

Prepared by:
Dr. Afsaneh Rabiei
North Carolina State University

***November 2014***

TRANSPORTATION RESEARCH BOARD
OF THE NATIONAL ACADEMIES

**Innovations Deserving Exploratory Analysis (IDEA) Programs**
**Managed by the Transportation Research Board**

This IDEA project was funded by the Safety IDEA Program.

The TRB currently manages the following three IDEA programs:

- NCHRP IDEA Program, which focuses on advances in the design, construction, and maintenance of highway systems, is funded by the American Association of State Highway and Transportation Officials (AASHTO) as part of the National Cooperative Highway Research Program (NCHRP).
- The Safety IDEA Program currently focuses on innovative approaches for improving railroad safety or performance. The program is currently funded by the Federal Railroad Administration (FRA). The program was previously jointly funded by the Federal Motor Carrier Safety Administration (FMCSA) and the FRA.
- The Transit IDEA Program, which supports development and testing of innovative concepts and methods for advancing transit practice, is funded by the Federal Transit Administration (FTA) as part of the Transit Cooperative Research Program (TCRP).

Management of the three IDEA programs is coordinated to promote the development and testing of innovative concepts, methods, and technologies.

For information on the IDEA programs, check the IDEA website (www.trb.org/idea). For questions, contact the IDEA programs office by telephone at (202) 334-3310.

IDEA Programs
Transportation Research Board
500 Fifth Street, NW
Washington, DC 20001

# *Materials with Improved Absorption of Collision Forces for Railroad Cars*

IDEA Program Final Report

For the period *09/2012* through *08/2014*

IDEA Project Safety-20

Prepared for the IDEA Program

Transportation Research Board

National Research Council

*Principal Investigator: Dr. Afsaneh Rabiei*

*North Carolina State University*

*August 2014*

## ACKNOWLEDGEMENTS

This research was supported by the National Academies' Transportation Research Board (TRB) IDEA Program. The project, "Materials with Improved Absorption of Collision Forces for Railroad Cars," is part of the Safety IDEA Program, which is funded by the Federal Railroad Administration. Charles Taylor was the TRB Project Manager.

The PI would like to express her sincere gratitude to Dr. Hyonny Kim and Dr. Daniel Whisler from The University of California, San Diego for their great effort on high-speed testing experiments and Dr. Addis A. Kidane and his team from University of South Carolina for providing access to their Split Hopkinson Pressure Bar. A team of graduate and undergraduate students, Youness Alvandi-Tabrizi (PhD student), Alexey Bukanov (MS student) and Davis Mooney (undergraduate student), have been actively working on this project and their efforts are acknowledged. Last, but not least is our sincere gratitude to the external review panel members Drs, Thomas Kurfess, Melisa Shurland, and Gunter Stephani for their time and attention providing many valuable comments during the course of this project.

## TABLE OF CONTENTS

## EXECUTIVE SUMMARY

The objective of this project was to examine the potential of Composite Metal Foams (CMFs) to improve the crashworthiness of railroad cars. Potential applications include the incorporation of CMFs into the structural members of passenger cars. Numerous efforts have gone into understanding the mechanical properties of metallic foams in general and CMFs in particular. While most of those studies have covered the properties of the material under a variety of low-speed loading conditions, this study extended the current knowledge by investigating CMFs' behavior under high-speed loading rates to mimic the speeds at which passenger cars and trains travel. For this purpose, the project team first optimized the CMF processing techniques in order to enable the processing of large-scale and low-cost CMFs. Then a Split Hopkinson Pressure Bar was used to investigate the mechanical performance of composite metal foams under high-speed impact speeds of 13, 22, and 30 m/s (equal to about 30, 50, and 68 mph). The results showed that elastic modulus, strength and total energy absorption of CMFs under such loading rates is significantly higher than those under quasi-static (slow) loading. This makes CMFs even more attractive for application in collision protection of railroad cars or other vehicles.

Studying samples with various sizes of preformed hollow spheres in the foam and different matrix material showed that as long as the wall-thickness to sphere-diameter ratio is kept constant, there is not much of a difference in mechanical properties of CMF samples made with different sphere sizes, particularly under low-speed loading. Such behavior is observed in both CMF samples with an aluminum matrix cast between steel spheres (Al-S CMF) and CMFs with a stainless steel matrix sintered between steel spheres (S-S CMF).

In the second set of high-speed loading experiments, mechanical properties of CMFs under higher strain rates between 60 to 120 mph were studied using Hopkinson bar experiments. While most high-speed loading tests were conducted at low strain levels, this study performed tests up to 50% strain.

The results indicated high strain rate sensitivity for both steel–steelsteel–steel CMF (processed through powder metallurgy) and aluminum–steel CMF (processed through casting) samples, especially at lower strain levels up to 30% strain. This leads to a significant improvement of the energy absorption capacity of CMFs at higher strain rates.

While the strain rate sensitivity of the parent material, micro-inertia effects and shock wave propagation may contribute to the strain rate sensitivity of CMFs, the strengthening at high strain rates is mostly attributed to the kinetics of entrapped air inside the spheres.

As can be seen in the project team's experimental data on samples with various sizes, the sample size effect on performance of CMFs under loading is very minimal. That means all of the experimental results from these small-scale studies are valid for the design of full-scale Crash Energy Management System (CEMS) prototypes.

Moreover, the project team's studies showed a great improvement in volume and weight savings while maintaining the same safety level, or dramatically improved safety levels, if the current weight of the CEMS of railroad cars is maintained by using steel–steel or aluminum–steel composite foams.

The results of these studies provide the project team with a wealth of knowledge about the properties of CMFs in different loading conditions with a variety of sizes and configurations, which is necessary for the design and manufacturing of full-scale CEMS prototypes. This information is very useful for the utilization of CMFs in the collision protection of railroad cars or other vehicles as well as for such applications as crushable workstation tables in passenger cars. Workstation tables in rail cars need to deform in a graceful manner to protect passengers sitting at the table, in accordance with American Public Transportation Association standards. The current crushable tables are heavy in comparison to regular tables, and require a substantial structure to support them. CMFs can provide light-weight and exceptional energy absorption that can resolve the current issue with such tables. Additional studies may be required to fine-tune the properties of CMFs for such applications. Moreover, the crash energy absorption, fatigue life, and thermal insulation properties of CMF have potential for tank car applications that deserve further assessment. CMF jackets between the walls of a double wall surrounding the tank could reduce the likelihood of a puncture of the tank in a derailment and as a thermal barrier to protect the tank contents in the case of a fire.

The technology for manufacturing CMFs is relatively easy to scale up, and can be retrofitted into any production line. Production requirements include a furnace, a shaking table and a mold, plus the raw materials and know how. However, the integration or retrofitting of the new material into any current passenger car (or tank car) structure would require some additional study. In previous work, the research team was able to scale up the processing of CMFs to produce larger one-foot by one-foot panels.

# 1 IDEA PRODUCT

## 1.1 INTRODUCTION

The Federal Railroad Administration's (FRA's) strategic primary goal for a national high-speed rail program is to ensure safe and efficient transportation choices by promoting the safest possible movement of goods and people, and optimizing the use of existing and new transportation infrastructure (*1*).

According to the FRA, the plan is to develop tiered passenger rail corridors that take into account the different markets and geographic contexts found throughout the United States. FRA defines four different speed classes for railroad cars (*2*)*:*

- "Core Express Corridors that would connect large urban areas up to 500 miles apart with 2–3 hour travel time and train speeds between 125 and 250 mph. Regional Corridors that would connect mid-sized urban areas, and smaller communities in between, with convenient, frequent, 90–125 mph service. Emerging/Feeder Routes that would connect regional urban areas at speeds up to 90 mph on shared track. Community Connections integrated with existing and future policies and

investments in public transportation, airports, and other modes to provide convenient options for accessing the passenger rail network."

High-speed requirements change the philosophy of design for safety devices and impose special requirements, specifically when it comes to designs for public transportation. As a result, scientists and engineers are working hard to develop advanced materials that can meet the new safety requirements, while simultaneously increasing their efficiency, improving fuel economy, and reducing costs for production and maintenance.

The ability to absorb energy in a crash by deforming the structure is a natural characteristic of today's vehicles. Part of the kinetic energy of a vehicle under impact will be transformed into its body deformation. According to the conservation of energy law, the more the vehicle deforms the higher energy absorption by its body and the lower the energy transferred to the passengers inside. The development of new advanced materials with increased energy absorption capabilities is necessary to further improve vehicle safety. Such materials must also have low enough density so that we can take advantage of the improved safety without increasing the vehicle weight and fuel consumption.

## 2 CONCEPT AND INNOVATION

Metal foams are a new class of materials offering an order of magnitude higher energy absorption under compression compared to the bulk materials that they are made of, and at an order of magnitude lower density (*3*). CMF has recently been highlighted in many scientific journals following the Science Nation (http://www.nsf.gov/news/special_reports/science_nation/metalfoam.jsp) article and video posted in January 2010 (*4*–*6*). This new type of metal foam is produced by filling the vacancies around a random loose collection of preformed hollow steel spheres with a solid matrix material by casting or powder metallurgy (PM) techniques (*4*) with the aim of increasing the foam's strength and energy absorption. Studies by the Principal Investigator have shown that the addition of the matrix strengthens and stabilizes the sphere walls, reducing the possibility of their buckling under loading and resulting in a stronger material with a much greater energy absorbing capability. The properties of composite metal foams can be altered by their processing technique, variation of the size and wall thickness of the hollow spheres as well as the matrix and sphere materials. By using preformed hollow spheres of known dimensions, the properties of the foam became more uniform and predictable. This new metallic foam has shown up to 7–8 times higher energy absorption compared to any other metal foam made from similar materials and many times higher energy absorption under loading compared to the bulk materials that they have been made of. For example, composite foam made 100% out of stainless steel can have a density of about 30% of the bulk steel (2.7 gr/cc, or as light as aluminum) while offering up to about two orders of magnitude higher energy absorption under mechanical loading/impact. This combination of properties holds the potential to revolutionize vehicle safety. The properties of metal foams in general and composite metal foams in particular have been studied under quasi-static and cyclic loading (*7*–*11*). However, the dynamic properties of the material under various impact speeds, matching those of potential railroad car collisions, had not

been examined; this was the purpose of this project. This project is necessary before the project team can implement their novel composite foam into the next generation of railroad cars.

It is notable that other mechanical properties of Al-S CMF and SS CMFs have already been evaluated experimentally in the project team's previous studies and are shown in Table 1. These properties include elastic modulus or stiffness, yield and maximum strength under four-point bending, and fatigue life. More detailed information can be found elsewhere (*8–10*). Under compression fatigue or cyclic loading, the composite foam samples show a high cyclic stability at maximum stress levels as high as 90MPa. Unlike other metal foams, the composite metal foams do not deform by rapid strain accumulation within collapse bands but, instead, by a uniform distribution of deformation through the entire sample. When compared to the regular Al foams, the Al–steel composite foams can endure higher cyclic stresses and exhibit longer fatigue lives due to the more uniform cell structure and the presence of the ductile matrix between individual spheres. The PM steel composite foams exhibit superior fatigue properties when compared to hollow sphere foams made from similar materials due to the high bonding strength between spheres and the presence of the matrix. The metallic matrix in all composite metal foams has the effect of strengthening the sphere walls under loading and reducing the likelihood of their buckling as well as blunting the crack tip significantly, decreasing the crack growth rate, preventing further collapsing of the neighboring spheres and leading to a more uniform deformation. The hollow spheres, on the other hand, provide a more uniform network of cells through the whole ensemble and prevent the formation of collapse bands and premature failure of the material.

TABLE 1 Other mechanical properties of CMFs (*8–10*)

| | Elastic Modulus (GPa) | Poisson's Ratio | Plateau Strength (MPa) | Compression Yield Strength (MPa) | 4-point Bending Yield (MPa) | Maximum Stress in Fatigue (MPa) | Fatigue Life x $10^6$ Cycles |
|---|---|---|---|---|---|---|---|
| Al-SS CMF | 11.9 | 0.36 | 90 | 58 | 55 | 44 | 1.42 |
| S-S CMF | 9–10.3 | 0.3 | 136 | 40 | 45 | 68 | 1.08 |

# 3 INVESTIGATION

This project consists of nine tasks; seven tasks in stage I, and two for stage II. The following sections present a summary of the steps taken for each task and the results.

## 3.1 STAGE I: PROCESSING CMF AND DYNAMIC TESTING AT VARIOUS IMPACT SPEEDS

### *3.1.1 Task 1: Preliminary design*

The main energy-absorbing component in currently used crush zone systems in railroad car structures is designed to have the ultimate energy absorption capacity of 2.7 MJ (*12–14*). The project team's goal is to

replace these components with a new design made out of composite metal foams (CMF). Considering the energy absorption per unit volume of a typical CMF (made of steel–steelsteel–steel combination) for 60% deformation (79 MJ/$m^3$), the necessary volume for absorbing the standard energy of 2.7 MJ can be calculated as:

$$V = \frac{2.7}{79} = 0.0342\ m^3 \quad (1)$$

Having a density of CMF of about 2.83 gr/cc, the mass of such volume of CMF will be:

$$M = 0.0342 \times 2.83 \times 1000 = 96.81\ kg \quad (2)$$

This is 82% of the mass of the currently used standard energy absorbers (which are large square tubes of steel) with 118 kg mass. If using the same amount of mass for CMF (118 kg), a volume of 0.042 $m^3$ would be needed. Energy absorption for this volume can be calculated as follows:

$$E = 0.042 \times 79.01 = 3.29\ MJ \quad (3)$$

This implies that with replacing the current standard primary energy absorption equipment with a cube shape block of steel–steel composite metal foam of the same weight, the energy absorption efficiency will be about 130%. Table 2 lists the energy absorption capabilities for different configurations of crash energy management systems compared to a typical composite metal foam made of steel–steel components. As can be seen, the steel–steel composite foam can provide a lighter configuration compared to the standard configurations in absorbing the standard 2.7 MJ of energy, while the volume occupied by it is much lower than all other configurations.

TABLE 2 Geometry and weight comparison of various primary energy absorbers with different configurations and a typical steel–steel composite metal foam block (*14*)

| E = 2.7 MJ | Pure Aluminum Foam | Empty Aluminum Tubes | Empty Steel Tubes | Foam-Filled Aluminum Tubes | Foam-Filled Steel Tubes | Standard Energy Absorber | Steel–Steel Composite Metal Foam |
|---|---|---|---|---|---|---|---|
| Weight (kg) | 325 | 125 | 111 | 94 | 80.4 | 118 | 96.81 |
| Volume ($m^3$) | 0.54 | 0.57 | 0.21 | 0.22 | 0.11 | 0.09439 | 0.0342 |

### *3.1.2 Task 2: Manufacturing of composite metal foams*

Composite metal foam (CMF) has been processed based on two basic processes: casting and powder metallurgy (PM). In the casting process, the hollow spheres and matrix materials were chosen to have distinctly different melting temperatures; specifically the matrix material must have a lower melting point than that of the sphere material so that the spheres will stay stable during casting. As a result, aluminum is selected for casting around steel hollow spheres. In the PM process, similar materials (like steel) can be used for both the matrix and spheres, because the processing temperature is maintained below the melting point of both components and there is no need to be concerned about the stability of either one of the components during processing. The advantage of using similar materials is that it leads to stronger bonding

between the matrix and sphere walls, and improves the strength of the final composite foam. On this basis, all CMF samples were produced from steel hollow spheres either in a steel matrix (S-S CMF) or in an Al matrix (Al-S CMF).

#### 3.1.2.1 Hollow spheres

The hollow spheres used in this project were produced by Hollomet in Germany, using a powder metallurgy process. All spheres were made of stainless steel (except that the carbon content is slightly higher than stainless steel) and have three major nominal outer diameter sizes of 2, 4, and 5.2 mm. The average outer diameter, wall thickness and porosity percentage of all spheres are presented in Table 3. The spheres are designed in a way to maintain a constant ratio of sphere wall thickness to outer diameter in all spheres and have a low percentage of porosities within the sphere walls. This was to make sure the samples were all uniform and that the resulting data would be repeatable and reliable.

TABLE 3 Geometrical characteristics of hollow spheres

| Outer Diameter (mm) | Wall Thickness (μm) | Porosity in the Wall |
|---|---|---|
| 2 | 90 | 3.4% |
| 4 | 196 | 6% |
| 5.2 | 244 | 4% |

As the project team's final goal is to be able to mass-produce these materials with reasonably low cost, the team tried to use some lower-cost mass-produced hollow spheres in this study and compare the properties of CMFs with those made with high cost laboratory produced hollow spheres that had been reported in the team's previous studies. Table 4 presents a comparison between the chemical and physical properties of the new low-cost hollow spheres with the old high-cost hollow spheres. As can be seen, the new hollow spheres have similar composition to 316L stainless steel with the exception of additional carbon content. This extra carbon content had an impact on the properties of both types of composite foam produced by PM and casting techniques. At the same time the sphere surface roughness and sphere wall porosity was higher in the new low-cost spheres. However, through some systematic approaches that are explained in the upcoming sections, the project team have managed optimizing the properties of CMFs processed using these low-cost spheres; in some cases the team even had better properties compared to their old samples that were produced with more expensive spheres.

TABLE 4 Comparison of the chemical composition for new and low-cost spheres used in this study and the high-cost spheres used previously

| Sphere Size | Chemical Composition (%) | | | | | | |
|---|---|---|---|---|---|---|---|
| | Fe | C | Mn | Si | Cr | Ni | Mo |
| New 2 mm | Balance | 0.68 | 0.13 | 0.82 | 16.11 | 11.53 | 2.34 |
| New 4 mm | Balance | 0.63 | 0.11 | 0.73 | 16.91 | 12.35 | 2.19 |
| New 5.2 mm | Balance | 0.87 | 0.07 | 0.34 | 17.09 | 12.60 | 2.12 |
| Old & Expensive 2 mm | Balance | 0.17 | 0.15 | 0.90 | 16.20 | 13.30 | 2.20 |
| Old & Expensive 3.7 mm | Balance | 0.03 | 0.2 | 0.9 | 17 | 13 | 2.2 |

#### 3.1.2.2 Steel–steel composite metal foam

The matrix material for the project team's PM CMF samples was 316L stainless steel produced by North American Hoganas High Alloys LLC. Two permanent molds were made from grade 304 steel and were used to produce S-S CMF samples. More details on processing of CMF using PM technique can be found elsewhere (*5*). Except for using bi-modal matrix instead of single-modal matrix as well as increasing the sintering temperature from 1200°C to 1250°C, all other processing steps are the same as what is reported in the project team's previous studies. More explanation on the team's motivations to make those modifications in the processing technique is coming up in the optimization section.

#### 3.1.2.3 Aluminum–steel composite metal foam

Aluminum 356 alloy was chosen as the matrix material for the project team's aluminum–steel composite metal foams processed by casting. This selection was due to the low density, high strength and stiffness, and ease of casting of Al 356 alloys. The main alloying elements in 356 aluminum alloys are silicon and magnesium, aiding in ease of casting and improving the strength of the matrix. Aluminum matrix was used together with steel spheres in order to maintain the structural stability of spheres during the casting of molten aluminum and to prevent the penetration of liquid metal into the cavities of the spheres.

The basic casting technique that is used is similar to the gravity casting method that is explained in the project team's previous study (*6*). However, since the gravity casting technique does not provide enough pressure to push the aluminum in between the spaces of the smaller spheres, it was not possible to make samples with 2 mm spheres. Hence, the casting technique was modified by adding a variable pressure system to provide better filling of the molten aluminum between the spaces of the smaller spheres.

The casting mold used is a permanent stainless steel mold with a sprue, runner, melt filter, and overflow riser. After pouring the liquid metal, pressurized air is injected through the sprue to force the molten aluminum to penetrate the small spaces between the hollow spheres (see Figure 1). Two cups are added on each side of the mold to collect any overflowed aluminum after the pressure is applied. The air pressure helped to push out any air trapped inside the mold and in between spheres, leaving the final sample with fewer voids and porosities in the matrix.

The system consisted of two pressure regulators, a custom steel cylinder insert, and rubber tubing. The steel cylinder was used as a connector to the sprue. Due to the high temperature of the mold during casting, the cylinder was placed inside an alumina ceramic cap in order to protect the rubber tubing and connectors from overheating. Shop air was reduced from 100 psi using two pressure regulators. The first regulator reduced the pressure to approximately 15 psi. The secondary, high-flow pressure regulator was used to control the incoming pressure during casting. When casting samples, the aluminum was first poured into the sprue. Then, the steel cylinder was inserted and pressure applied. The pressure was increased gradually until the aluminum passed through the entire mold cavity. With the casting process completed, the mold was air cooled with shop air until the temperature of the mold walls reached 200°C, after which

the mold was left to cool down gradually in air. More details on the processing of aluminum–steel CMFs through gravity casting without any air pressure are explained in the project team's previous reports (*6, 7*).

#### 3.1.2.4 Samples preparation

Once the samples cooled and were removed from both the casting and PM molds, they were cut into desired lengths using a Buehler Isomet equipped with a diamond wafering blade. A diameter-to-length ratio of 0.7 was maintained in all cut samples. The size of each sample was selected to be large enough to avoid free edge effects; i.e., to have at least six spheres along the diameter of the sample. A center hole was drilled in a number of S-S and Al-S CMF samples with 4 mm spheres using milling bits to fabricate hollow cylindrical samples with inner-to-outer diameter ratios of 1/3. All samples were subjected to density evaluation by accurate weighting and dimensional measurements.

A total of 203 CMF samples were manufactured, cut and tested in various steps of this project. Table 5 shows the number of different samples made for this project. A portion of these samples that were made using powder metallurgy and casting techniques with different sphere sizes are illustrated in Figure 2. More details about size, density and other specification of the samples are presented in upcoming sections of this report. Nominal dimensions of the samples along with their average density are presented in Tables 6–9.

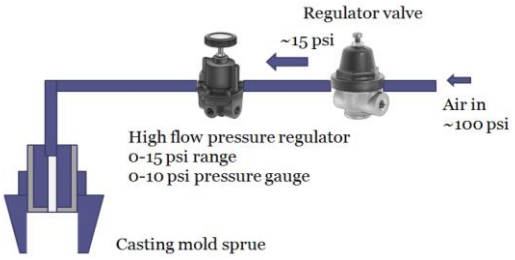


**FIGURE 1** Diagram of the air flow system added to the gravity-casting mold for better penetration of air between hollow spheres.

TABLE 5 Number of composite metal foam samples made during the course of this project

| Samples Made for | Number of Samples |
|---|---|
| Optimization of PM samples, quasi-static loading | 20 |
| PM samples for quasi-static tests | 9 |
| PM samples for medium-speed tests | 68 |
| PM samples for high-speed tests | 45 |
| Optimization of casting | 25 |
| Casting samples for quasi-static tests | 9 |
| Casting samples for high-speed tests | 27 |

**FIGURE 2** A portion of untested samples made using powder metallurgy (left half of the picture) and casting (right half of the picture) techniques with different spheres size.

TABLE 6 Nominal dimensions of cylindrical S-S CMF samples along with their average density

| Sphere Size | Diameter (mm) | Length (mm) | Density (gr/cm$^3$) |
|---|---|---|---|
| 2 | 25.4 | 17.78 | 2.85 |
| 4 | 25.4 | 17.78 | 2.79 |
| 5.2 | 38.1 | 26.67 | 3.06 |

TABLE 7 Nominal dimensions of cylindrical Al-S CMF samples along with their average density

| Sphere Size | Diameter (mm) | Length (mm) | Density (gr/cm$^3$) |
|---|---|---|---|
| 2 | 25.4 | 17.78 | 1.95 |
| 4 | 38.1 | 26.67 | 1.94 |
| 5.2 | 38.1 | 26.67 | 1.96 |

TABLE 8 Nominal dimensions of hollow cylindrical S-S CMF samples along with their average density

| Sphere Size | Outer Diameter (mm) | Inner Diameter (mm) | Length (mm) | Density (gr/cm$^3$) |
|---|---|---|---|---|
| 4 | 25.4 | 8.47 | 17.78 | 2.81 |

TABLE 9 Nominal dimensions of hollow cylindrical Al-S CMF samples along with their average density

| Sphere Size | Outer Diameter (mm) | Inner Diameter (mm) | Length (mm) | Density (gr/cm$^3$) |
|---|---|---|---|---|
| 4 | 25.4 | 8.47 | 17.78 | 1.90 |

In order to have a proper surface finish for microstructural observation, one side of each sample was ground and polished progressively using 180–1200 grit papers and 3 µm diamond slurry in Buehler AutoMet 2 Power Head grinding and polishing stations at 150 rpm followed by polishing using a 9 and 3 µm diamond suspension, and a 1, 0.1, and 0.05 µm alumina-water polishing compound on polishing cloths.

### *3.1.3 Task 3: Preliminary studies of the CMF samples*

Digital images taken from the cross section of S-S and Al-S CMF samples are shown in Figures 3a–3f. The nearly uniform and regular structure of CMF is evident in these images. Except for a few spheres in the Al-S CMF sample with 5.2 mm spheres that were de-bonded during the cutting and grinding processes, all other spheres were well bonded to the matrix. It should be noted that since the cut did not pass through the center of all spheres, their diameters and wall thicknesses do not appear as their real size in all spheres.

Scanning Electron Microscopy (SEM) images shown in Figures 4a–4f show how spheres are bonded to the matrix. The presence of micro-porosities within the sphere wall of both S-S and Al-S CMFs can be seen in these figures. Other features that are shown include the porosities in the matrix of the S-S CMFs and intermetallic phases in Al-S CMFs. These residual porosities in S-S CMFs are caused by lack of full powder compaction in samples processed using the powder metallurgy technique (*5*). The percentage of porosities is calculated using image processing and is listed in Table 10. Comparison of these results with those obtained in previous studies using high-cost spheres reveal lower porosity in the matrix as a result of using a bi-modal matrix (*5*). However, since the porosity in the sphere walls was higher than that of previously used spheres, the final density of the samples was slightly lower.

TABLE 10 Porosity percentages in the matrix of all S-S CMF samples evaluated using image analysis along with their measured density

| Sphere Diameter (mm) | Matrix Porosity (%) | Measured Density (gr/cm$^3$) |
|---|---|---|
| 2 | 31.59 | 2.85 |
| 4 | 28.20 | 2.79 |
| 5.2 | 18.00 | 3.05 |

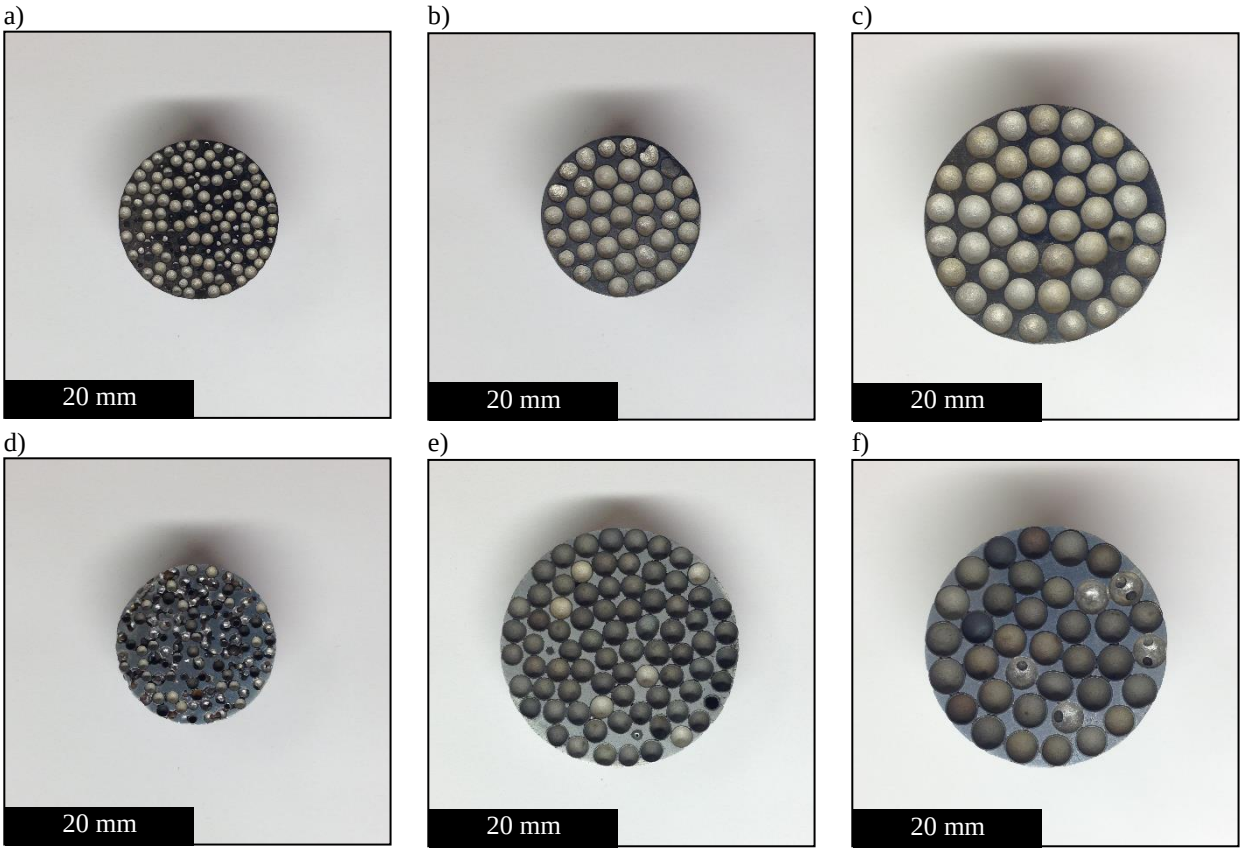


**FIGURE 3** Optical images taken from S-S CMF (a, b, and c) and Al-S CMF (d, e, and f).

As indicated by Figure 4 (and also Table 10) more porosity can be found in the matrix of S-S CMF made with 2 mm spheres, which can be due to the smaller spacing between such small spheres that made it more difficult to fully compact the matrix powder in those areas. It is notable that samples made

with 4 and 5.2 mm spheres did not show such rate of porosities in their matrix. That is due to the fact that there is enough spacing between larger spheres to allow for better compaction of the matrix powder in between spheres.

The SEM images in Figure 4 also show a good bonding between the spheres and matrix of Al-S CMF. Formation of intermetallic phases can also be seen at the sphere–matrix interface in all aluminum–steel composite foams. These are ternary intermetallic phases that formed between aluminum, iron and silicon as a result of inter-diffusion of atoms between the sphere wall and the matrix. These intermetallic phases are classified into three different categories—a layer immediately surrounding the sphere wall, a subsequent layer of plate-shape precipitations and a needle-shaped phase distributed within the matrix. Depending on the sphere size and composition, the intermetallic phases that can be seen in SEM images may have different shapes, sizes and distributions. The Principal Investigator's previous reports (*6–11*) contain more comprehensive discussions on microstructure and composition of intermetallic phases in Al-S CMF.

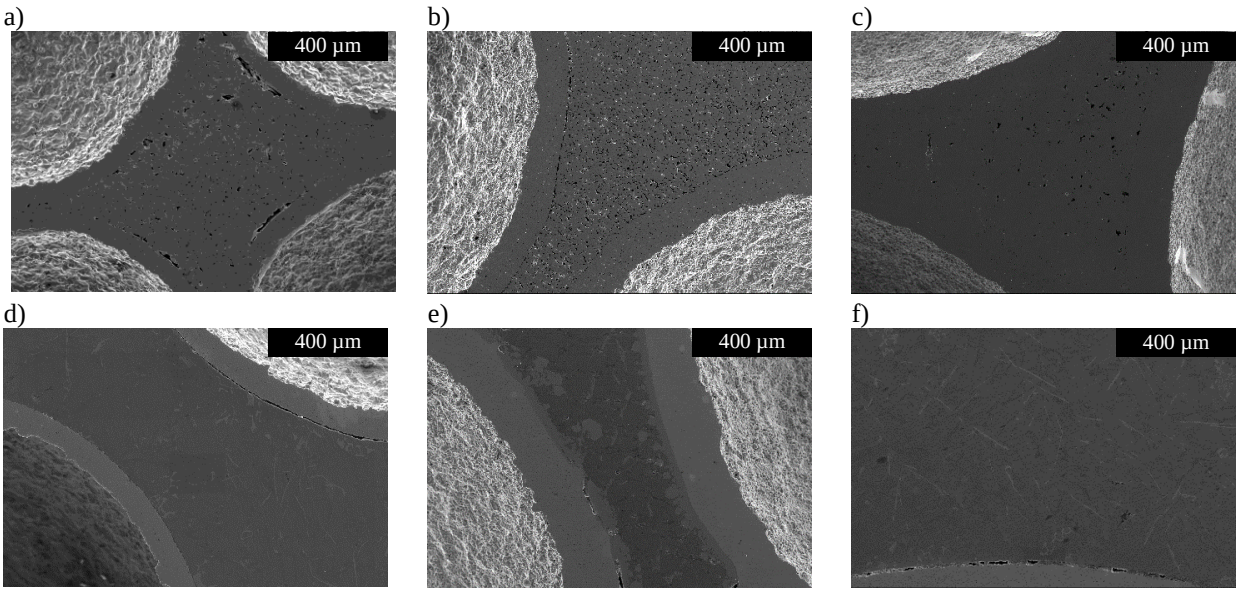


**FIGURE 4** SEM images taken from S-S CMF (a, b, and c) and Al-S CMF (d, e, and f).

*3.1.4 Task 4: Evaluation of mechanical properties of the CMF samples under low-speed loading*

Quasi-static compression tests were performed using a MTS 810 servo-hydraulic universal testing machine with a 980 kN load cell and a crosshead speed of 1.25 mm/min. These tests were conducted at the Construction Facilities Laboratory (CFL) at NC State University. Each measurement was repeated at least three times. The average of three measurements is reported here. It is notable that the standard deviations in the mechanical properties of CMFs made with more expensive spheres were in the range of 2.9% to 3.1% and that of new samples made with low-cost spheres were in the range of 5.66% to 9.34% depending on the sphere diameter and processing technique. After comparing the results from samples made with new low-cost spheres to those from previous studies, made with lab-scale and more expensive spheres, on both types of PM and cast CMFs, the project team noticed that the compression test results of their recent samples

show lower mechanical properties. The only reason for such discrepancy could be related to the change from high-cost lab-scale hollow spheres to the low-cost mass-produced hollow spheres. Figures 5 and 6 show a comparison between the stress–strain curves of the original samples made with very expensive lab-scale hollow spheres, with the new low-cost spheres before optimization of casting (Figure 5) and PM techniques (Figure 6). The first task for the project team was to evaluate the differences. In this case, the team learned that:

I. The carbon content of new low-cost spheres is much higher than expected, which caused more hardness and less ductility in spheres and the resulting CMF manufactured with those spheres. In order to balance this issue, the heating cycle was modified and the sintering temperature was increased from 1200ºC to 1250ºC in CMF processed using the PM technique. This allowed a better diffusion of carbon into the low carbon stainless steel matrix and a better balance of the composition between spheres and the matrix. Since there is a total of 16% sphere-wall material in the CMF structure in general with 40% matrix material and 46% air, the effect of extra carbon content in the sphere wall after being well diluted by the low carbon content of the matrix will become minimal. That is why the project team increased the processing temperature to further facilitate the migration of extra carbon from the sphere wall into the matrix, balance out the carbon content, and achieve more uniform mechanical properties, as can be seen in comparing Figures 6 and 8. In the case of cast CMFs, the additional carbon content had more severe effects on the mechanical and microstructural properties as can be seen in Figure 5. In that case, the higher carbon content in the sphere wall resulted in a higher amount of hard carbides precipitation in sphere walls, as well as a higher percentage of intermetallic phases present in the matrix, which would cause a hardening effect on the foam. The hard and brittle nature of the carbide and intermetallic phases causes an increase in the yield strength and an immediate drop after yielding (Figure 5). But, as can be seen in Figure 7, the optimization efforts could help to maintain the quality of CMFs even using low-cost hollow spheres with high carbon content.

II. The other issue was related to the higher surface roughness of the new low-cost spheres. This high surface roughness caused air trapping in between spheres and the matrix during processing. This issue prevented a good bonding between the matrix and spheres. In order to resolve this issue in cast CMF samples, a pressurized casting is used instead of gravity casting and in PM samples a bimodal matrix powder was utilized. That means, instead of single modal powder with constant particle size of 44 μm, bi-modal powder, which is a mixture of two different particle sizes of 149 μm (75%) and 44 μm (25%) was used.

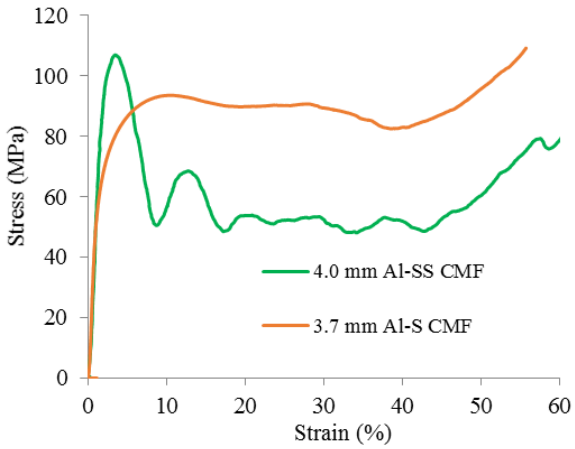


**FIGURE 5** Comparison of stress–strain curves for aluminum–steel cast samples made with 4 mm high-cost spheres (brown) and that of un-optimized cast samples made with the similar size but lower-cost spheres (green).

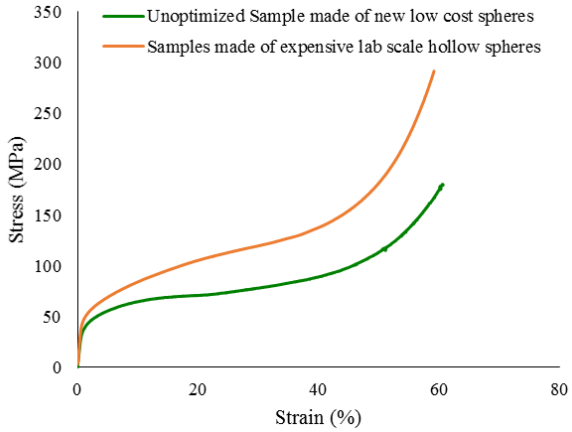


**FIGURE 6** Comparison of stress–strain curves for steel–steel CMF samples made with PM technique and 2 mm high-cost spheres (brown) and that of un-optimized PM samples made with the similar size but lower-cost spheres (green).

### *3.1.5 Task 5: Optimization*

The lower mechanical properties of samples made with the project team's new low-cost spheres necessitated some optimization of the team's processing technique. Since the sphere wall occupies only 16% of the total volume of CMF with the matrix occupying 40% and the rest occupied by air, it made sense for the project team to focus their optimization efforts on improving the properties of the matrix. As a result, the project team aimed their efforts at reducing the porosity percentage in the matrix and improving the bonding strength between the matrix and spheres. All samples were tested under quasi-static loading to confirm the effectiveness of the team's optimization efforts. The size of each sample was selected to be large enough to avoid free edge effects; i.e., to have at least six spheres along the diameter of the sample. Figure 6 also demonstrates that the sphere size does not have much of an impact on the mechanical properties of CMFs under quasi-static loading. Of course, this statement is only valid when the ratio of the

sphere wall thickness to its outer diameter is maintained constant in all spheres. An additional sphere size effect on the properties of aluminum–steel CMF made by casting is related to the surface contact between the spheres and the matrix that causes the formation of different amounts of hard and brittle intermetallic phases. This percentage is normally larger in CMFs made with smaller spheres, causing an additional initial strength and lower ductility, which eventually balance the total energy absorption of the CMFs under loading. As a result, this effect is also minimal on mechanical properties of CMF samples made with 2 mm spheres compared to those made with 4 and 5.2 mm spheres.

Figure 7 shows the stress–strain curves for aluminum–steel cast samples after optimization. It can be seen that the properties of new samples after optimization are improved quite a bit and matched those of the old samples made with more expensive spheres. This will be very useful in scaling up the technology for commercialization and real world applications. It is notable that prior to this study, the project team had not tested the 2 mm aluminum–steel cast CMFs due to the difficulty in filling the small gaps between such small spheres with highly viscose molten aluminum. However, in this project, the application of pressurized casting allowed the team to produce aluminum–steel foams by casting molten aluminum around 2 mm steel spheres for the first time. Each experiment was repeated at least three times. The average of all measurements is reported here.

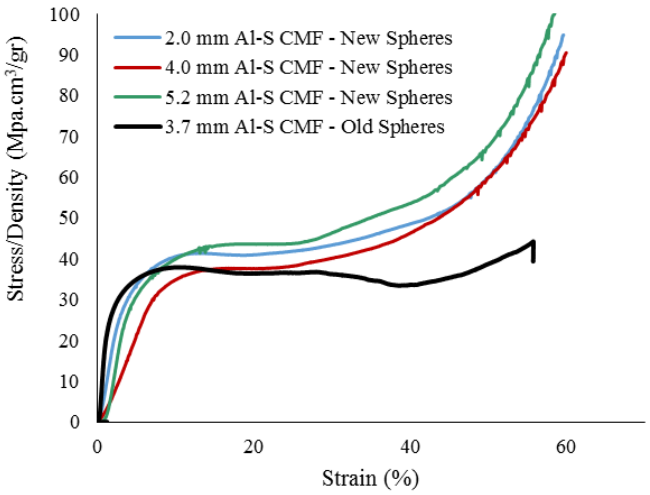


**FIGURE 7** Comparison of stress–strain curves for aluminum–steel cast samples made with 2, 4, and 5.2 mm low-cost spheres after optimization of processing.

The quasi-static compression test results on samples made during the optimization of the powder metallurgy technique are shown in Figure 8 for different processing parameters. Compression test result for the sample processed in previous studies with very expensive lab-scale hollow spheres is also included for comparison. The gradual improvement in stress–strain behavior of CMF by changing the processing parameters is clear from Figure 9. The optimization was sufficiently successful that the project team could even exceed the properties of samples previously processed with more expensive spheres.

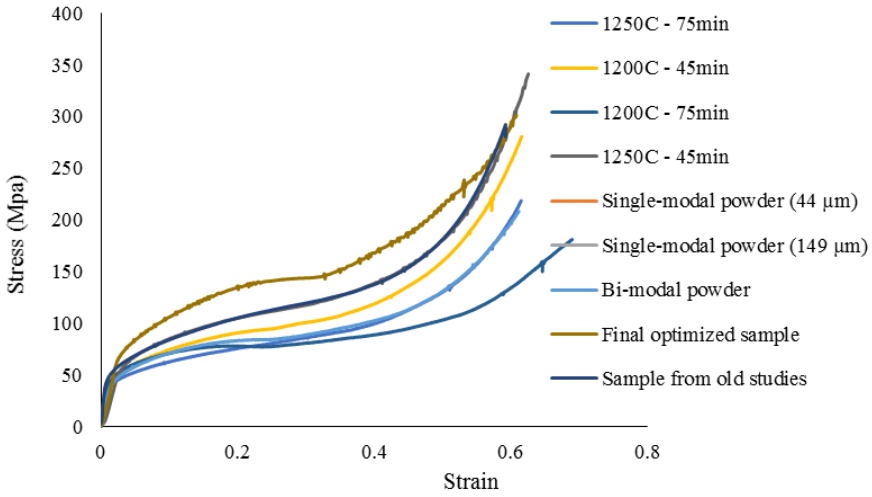


**FIGURE 8** Quasi-static compression test results through the optimization of powder metallurgy technique. The test result for samples processed in old studies is also included for comparison.

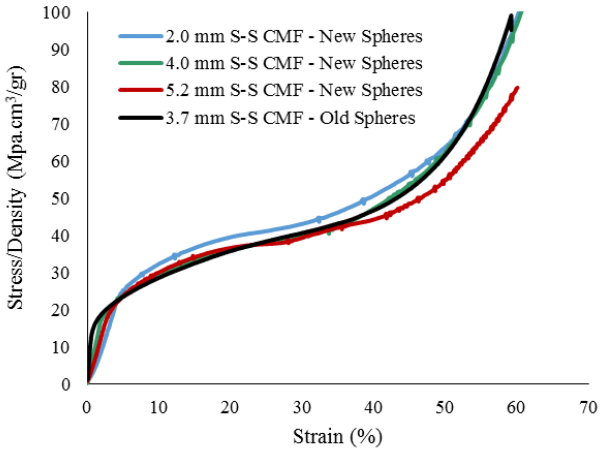


**FIGURE 9** Comparison of stress–strain curves for steel–steel CMF samples made with PM technique out of 2, 4, and 5.2 mm low-cost spheres after optimization of processing.

### *3.1.6 Task 6: High-speed impact test using Split Hopkinson Pressure Bar and Direct Impact Hopkinson Bar*

After the optimization of the process for fabricating CMF samples, two sets of high-speed tests were performed to assess the mechanical properties of CMF under high-speed and medium-speed loading. The first set was conducted at University of South Carolina for medium-speed impacts up to 30 m/s (67 mph) and the second one at University of California—San Diego for higher-speed impacts up to 120 m/s (268 mph).

3.1.6.1 High-speed impact test using Split Hopkinson Pressure Bar up to 30 m/s loading rate

The first set of high-speed tests was performed at the University of South Carolina using their Split Hopkinson Pressure Bar (SHPB) (see Figure 10). These tests were designed to study the loading rate and sample sizes effects on the performance and properties of composite metal foams. In this case, 68 cylindrical samples were prepared using the optimized PM technique with steel hollow spheres of 2 mm outer diameter embedded in a stainless steel matrix. After sintering the samples, their outer surfaces were machined using a center lathe to make two batches of samples with 22.86 mm outer diameter (called 1in. sample) and 14.6 mm outer diameter (called 5/8 in. sample).

As shown in Figure 11, the SHPB consists of a striker bar, an incident bar and a transmitted bar. A gas gun fires the striker bar and accelerates it to hit the incident bar, which then transfers the stress waves into the sample. A part of these stress waves is reflected back from the sample to the incident bar and the other part passes the sample and transmits into the transmitted bar after deforming the sample. The pressure of the gas gun along with the dimensions and material of the striker bar are the factors that control the impact speed. A high-speed camera was used to capture the impact of the striker bar with the sample (see Figure 12).

The gas gun was set to fire the 18-inch striker bar with pressures of 20, 40, 60, and 100 psi. The corresponding impact speeds for those pressures are 13, 19, 22, and 30 m/s, respectively. The maximum speed was equivalent to 68 mph, which is within the range of typical train speeds (*12*).

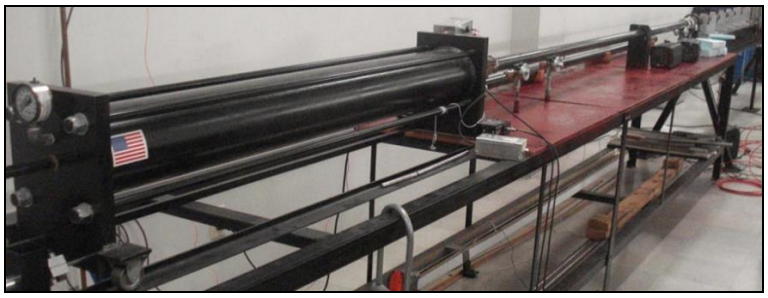

**FIGURE 10** Split Hopkinson Pressure Bar used in this experiment.

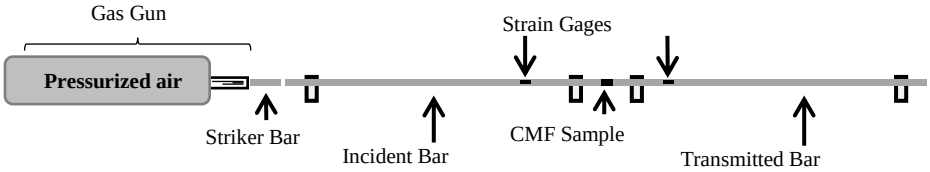


**FIGURE 11** Schematic illustration of the Split Hopkinson Pressure Bar.

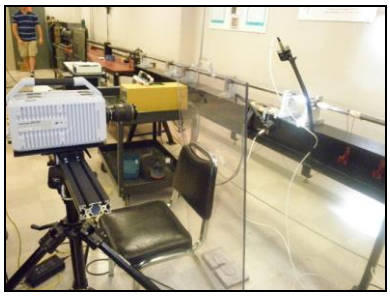

**FIGURE 12** A high-speed camera records the CMF samples crushed under dynamic loading in a Split Hopkinson Pressure Bar.

The results from quasi-static and dynamic compression tests are shown in Figure 13. It is notable that due to the high strength of the CMFs and the limited capacity of the Split Hopkinson Pressure Bar (SHPB), it was not possible to attain deformations beyond 20% strain. As can be seen in Figure 13, increasing the loading rate causes increases in the strength and elastic modulus of CMFs. Such behavior in CMFs results from the resistance of the air trapped inside the hollow spheres, micro-inertial effects, strain rate-sensitivity of the parent material, and shock wave propagation (*15*).

The optical images taken by the high-speed camera from the CMF samples at different strain levels during the dynamic compression test are shown in Figure 14. It can be seen that the CMF deforms nearly uniformly without any localized deformation bands. This is due to the utilization of hollow spheres in the structure of CMFs, which provides a uniform cell shape and size in the metallic foam and increases the strength by involving the entire material in load bearing and is one of the main advantages of composite foams compared to other types of metallic foams.

The amount of energy absorbed during deformation of the samples is obtained by calculating the area under the stress–strain curve. This is shown in Figure 15 for different loading rates at 6% strain. Improving the energy absorption by increasing the loading rate can be clearly seen in these figures. It is also noted that the comparison of results for 5/8 in. and 1 in. diameter samples demonstrates that the sample size has no effect on strain rate sensitivity and the performance of CMFs under various loading rates. This can be useful for predicting the properties of CMFs for application in a large-scale structural member.

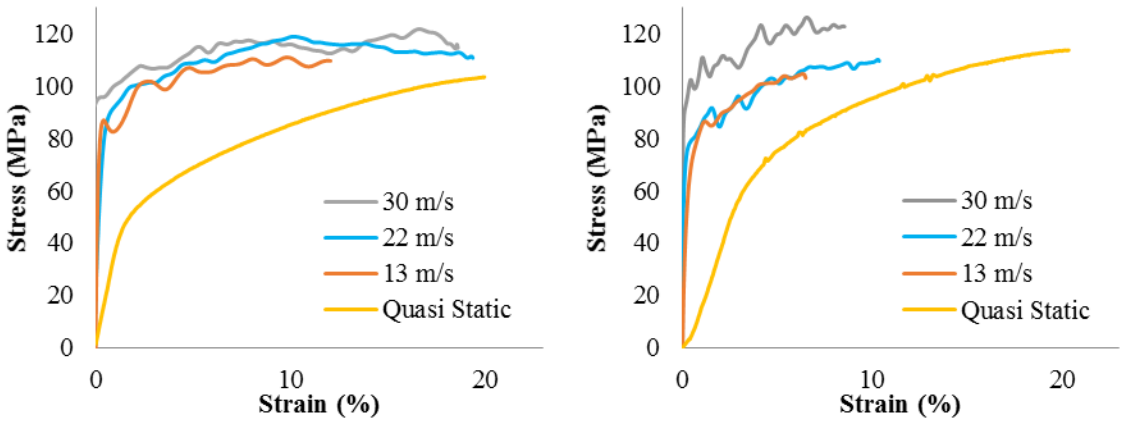


**FIGURE 13** Stress–strain behavior of steel–steel CMF samples under different loading rates; (*left*) 5/8 in. and (*right*) 1 in. diameter samples.

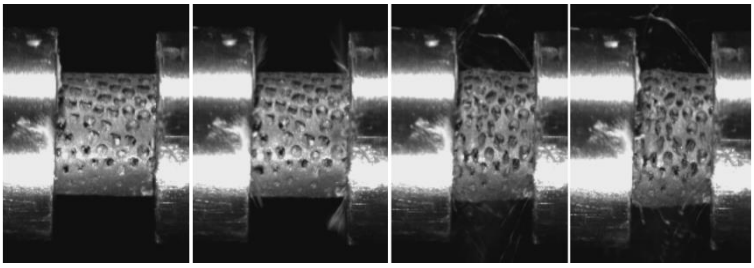

**FIGURE 14** High-speed camera images showing the deformation of steel–steel CMF under high-speed impact at different strain levels from left to right.

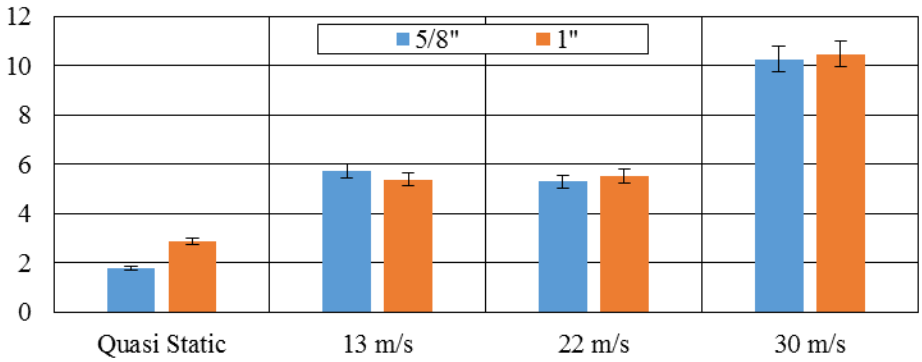


**FIGURE 15** Energy absorption per unit volume of steel–steel CMF (MJ/m$^3$) under different loading rates up to 6% strain.

3.1.6.2 High-speed impact test using Direct Impact Hopkinson Bar at impact rates above 30 m/s and up to 120 m/s impact velocities.

The second set of high-speed loading tests was conducted using a Direct Impact Hopkinson Bar at the University of California, San Diego. For this purpose, 45 PM samples and 30 casting samples with sphere diameters of 2, 4, and 5.2 mm were tested. In addition, six hollow samples were included in the

experiments. These tests were conducted to evaluate the properties of CMFs under high-speed loading from 88 m/s to over 160 m/s (equivalent to about 200 to 360 mph) to mimic the speeds at which high-speed trains could travel. The samples' dimensions were either 25 mm in diameter and 18 mm height for CMF samples with 2 and 4 mm spheres, or 37 mm diameter and 26 mm height for CMF samples made with 5.2 mm spheres. These were all steel–steel CMF made using the powder metallurgy (PM) technique. The test setup used an aluminum-faced foam projectile with an embedded steel plate that first impacted a transmission shaft and then impacted the CMF samples. Table 11 shows the projectile velocity, projectile mass and shaft mass corresponding with each strain rate for various samples used in this study.

TABLE 11 Projectile velocity, projectile mass, and shaft mass corresponding with each strain rate

| Strain Rate (1/s) | 3728 | 2740 | 2629 | 1982 | 1651 | 1523 | 1481 | 1345 | 899 | 653 |
|---|---|---|---|---|---|---|---|---|---|---|
| Projectile Velocity (m/s) | 164 | 119 | 117 | 88 | 147 | 120 | 120 | 120 | 95 | 117 |
| Projectile Mass (g) | 299 | 306 | 302 | 304 | 296 | 207 | 303 | 304 | 242 | 362 |
| Shaft mass (g) | 268 | 269 | 268 | 269 | 483 | 476 | 483 | 483 | 178 | 504 |

The gas gun and Hopkinson bar setups used tuned projectiles to dynamically impact test specimens up to 76 mm in diameter. The system is capable of accelerating the 300 g projectile at velocities up to 160 m/s with the 3.2 meter long aluminum Hopkinson bar, permitting up to 1.1 milliseconds of dynamic force data collection. The projectiles were custom-designed to impart a high impulse, short time duration pulse, by utilizing a 3.13 mm thick aluminum front face with a 51 x 51 x 6.35 mm thick steel backing mass cast at the tip of a 76 mm diameter foam projectile.

For this investigation, a 140 g aluminum shaft was polished and slid inside a low friction bronze sleeve bushing, while at the front of the shaft was a 25.4 mm thick 7075 aluminum disc designed to withstand repeated hits (Figure 16). Sandwiched between the two components were low-strength aluminum washers, which would deform plastically after the initial impact event. The 480 g intermediate shaft system applied a linear and planar loading surface for dynamic testing of the 25 mm and 37 mm diameter CMF specimens at speeds up to 120 m/s with specimen crushing up to 50% strain.

The test setup is shown schematically in Figure 17. The gas gun was pressurized to 3.3 MPa with nitrogen and the ball valve actuator was pressurized to 1.0 Pa with helium (see Figure 18). A Picoscope 3204 4-channel digital acquisition system received input from a dual laser velocity measurement system and a Vishay 2300 signal amplifier connected to dual 1000 Ω strain gauges installed on the Hopkinson bar. The two Phantom V7.3 high-speed cameras were set to independently record the projectile flight at wide angle (resolution 600 x 208, 20,000 fps and 8 μs exposure) and the specimen at close-in view (resolution 208 x 64, 111,000 fps, and 1 μs exposure).

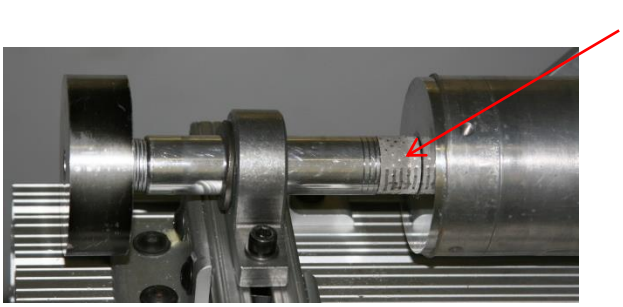


**FIGURE 16** Intermediate shaft assembly with CMF specimen loaded and ready to test.

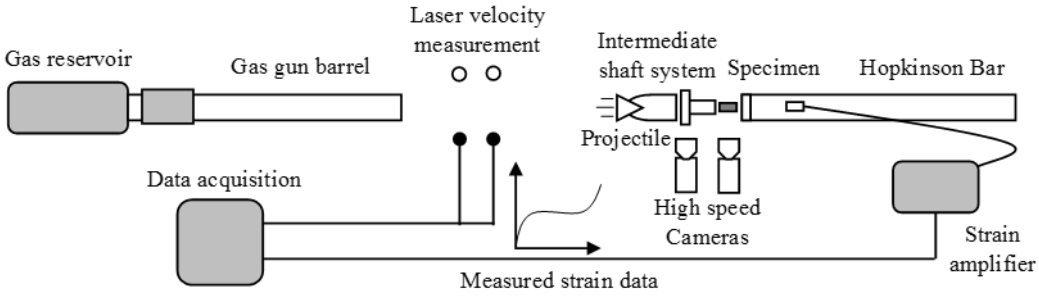


**FIGURE 17** High-speed test setup overview.

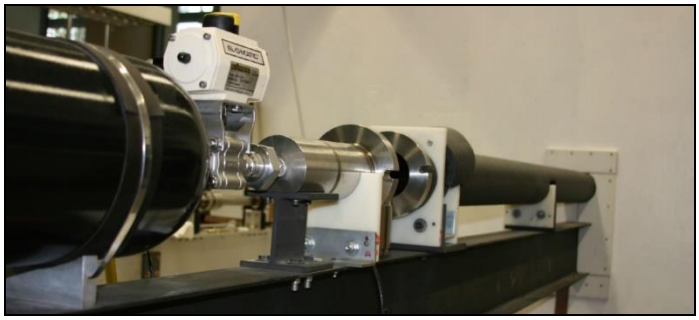

**FIGURE 18** Gas gun system.

The test procedure begins with the loading of the specimen. A small quantity of vacuum grease is applied to both faces of the specimen, which is then centered between the shaft and Hopkinson bar (Figure 16). The grease applies sufficient strength to hold the specimen in place with no additional support. The projectile is then loaded and the breech closed. Both cameras and data acquisition system are armed and the gas gun is pressurized to the predetermined 3.3 MPa. The ball valve is then triggered, accelerating the projectile through the velocity measurement box before impacting the shaft and specimen (see Figures 19 and 20).

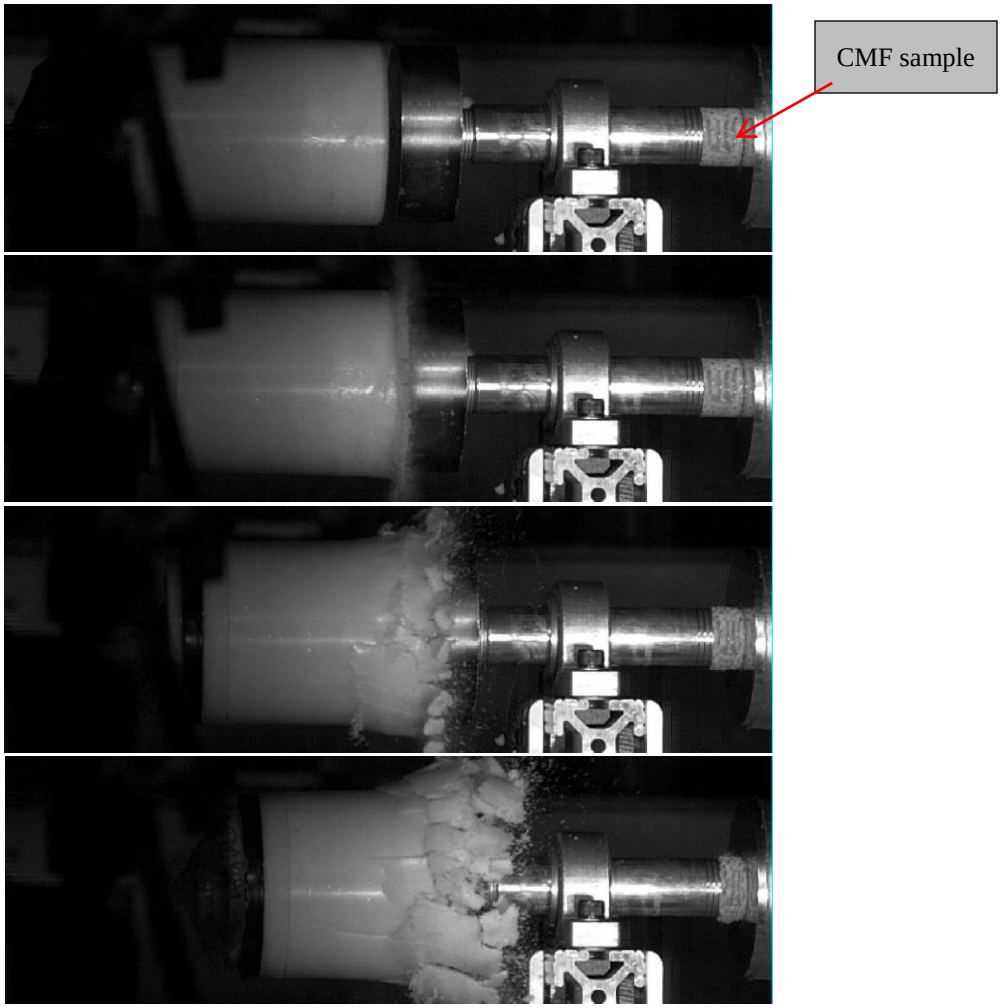


**FIGURE 19** Wide angle high-speed camera view of impact event for CMF specimen showing (from top) just before impact at $t = -87$ µs, projectile contacting intermediate shaft at $t = 13$ µs, progressive crush of projectile at $t = 213$ µs and completed crush at $t = 513$ µs.

Data from the Hopkinson bar and high-speed camera video were saved for further processing and the system was reset for the next test. The force-time history results were obtained directly from the Hopkinson bar data using the following conversion factor for dual strain:

$$F = EA\frac{2V}{G_F G_A E_v} \tag{4}$$

where $E$ and $A$ are the modulus (70 GPa) and cross sectional area (1390 mm$^2$), respectively, $V$ is the voltage output of the strain amplifier, $G_F$ is the gage factor (2.08), $G_A$ is the gain (100), and $E_v$ is the excitation voltage (10 V). Dividing the force data by the specimen cross-sectional area gives the stress-time history. It is notable that the time data is shifted such that the start of the loading curve corresponds to zero time.

The displacement data were processed manually from the high-speed video at 10 μs intervals with 0.13 mm resolution (pixel spacing based on the resolution and zoom of the Phantom camera). The data were then up-sampled to match the time scale and increments of the force data and time shifted such that the start of the loading curve corresponds to time zero. The strain-time history is then obtained by subtracting the displacement data from the initial size of the specimen. Finally, with both stress and strain calculated against a common time vector, the two quantities are plotted to obtain the stress–strain curve for the specimen. Figure 21 shows the PM samples before and after high-speed impact.

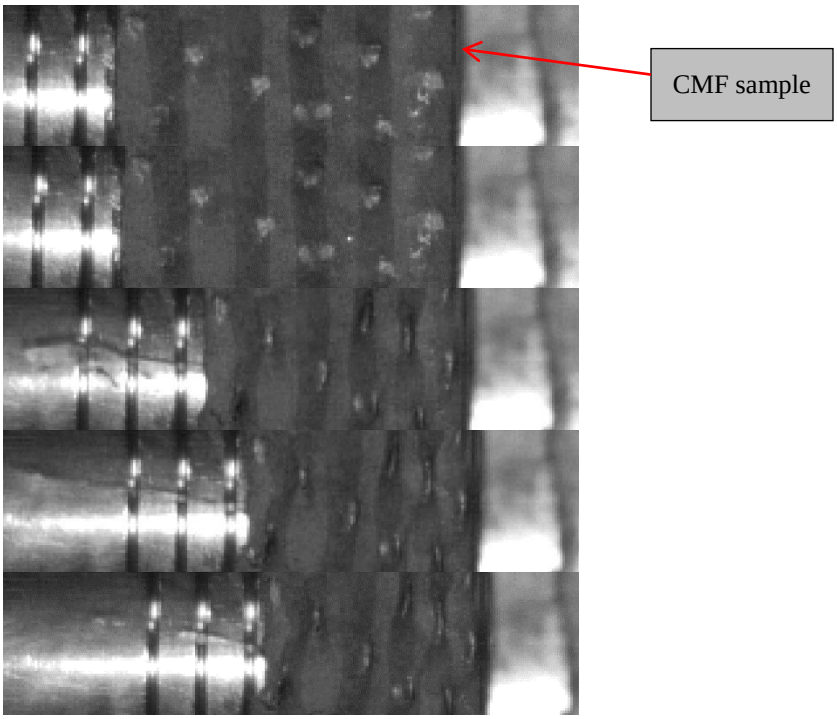


**FIGURE 20** Close up image of high-speed camera used during high-speed impact of CMF showing progression of specimen crush (from top) starting from impact at $t$ = 0 μs, $t$ = 18 μs, $t$ = 216 μs, $t$ = 369 μs, and full crush at $t$ = 513 μs.

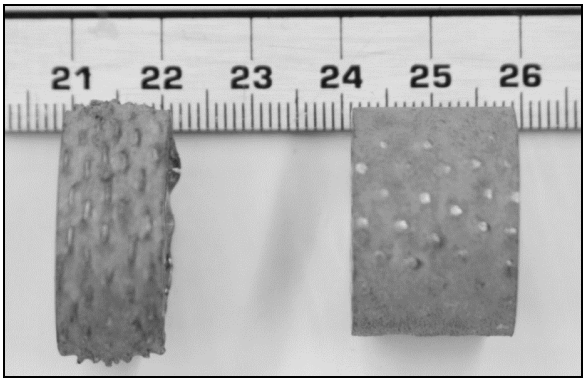


**FIGURE 21** CMF samples with 4 mm spheres processed through powder metallurgy technique before and after high-speed tests.

The stress strain graphs for these samples are shown in Figures 22 and 23. The effect of strain rate on samples made with 2, 4, and 5.2 mm spheres is shown in Figures 22a–22C and 23a–23C. In these graphs, the higher the strain rate, the higher the yield strength of the CMF, causing higher total energy absorption of the material. The observed strain rate sensitivity of CMFs confirms their potential for application in collision protection in railroad cars. For example, the yield strength of the steel–steel CMF samples was about 50–60 MPa in quasi-static loading, but increased to 150 MPa at higher loading rates of about 120 m/s. This shows an improvement of up to 200% in yield strength of the material when increasing the loading rates, and can be directly translated into higher energy absorption capability of the material at higher speeds of impact. Twelve percent to 22% improvement in the amount of energy absorption was achieved by increasing the loading rate to 2728 l/s. Comparison of the high-speed loading test results for samples with 2 and 4 mm spheres are depicted in Figures 22d and 23d. It is clearly seen that sphere size has a small effect on dynamic behavior of CMF. However, when moving towards the CMFs made with 5.2 mm spheres, the difference is more visible. Such difference was not observed in quasi-static loading of CMFs and is only a property of the material at high-speed loading. This effect will be further discussed in future sections.

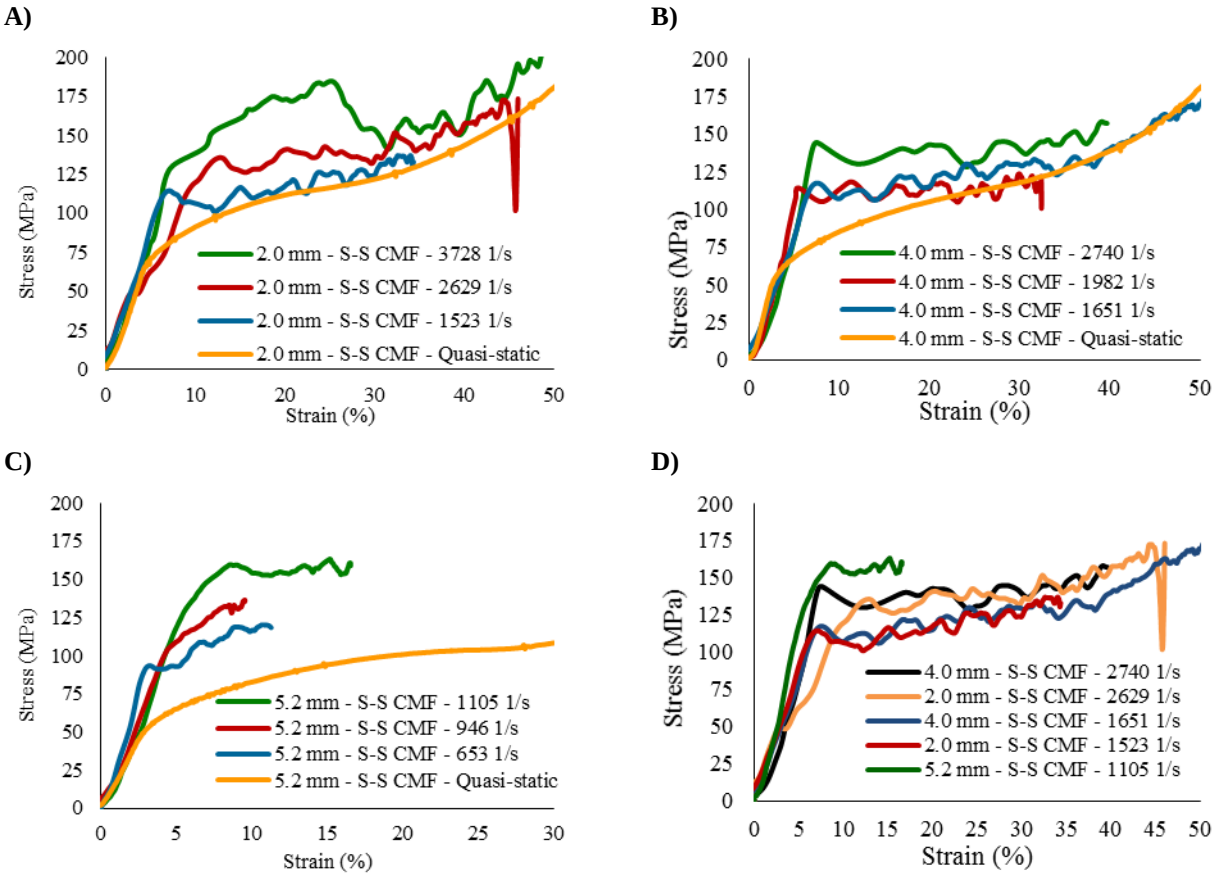


**FIGURE 22** Comparison of high-speed and quasi-static test results for S-S CMF samples at different loading rates: A) Samples with 2 mm spheres; B) Samples with 4 mm spheres; C) Samples with 5.2 mm spheres; D) comparison of results for samples with 2 and 4 mm spheres.

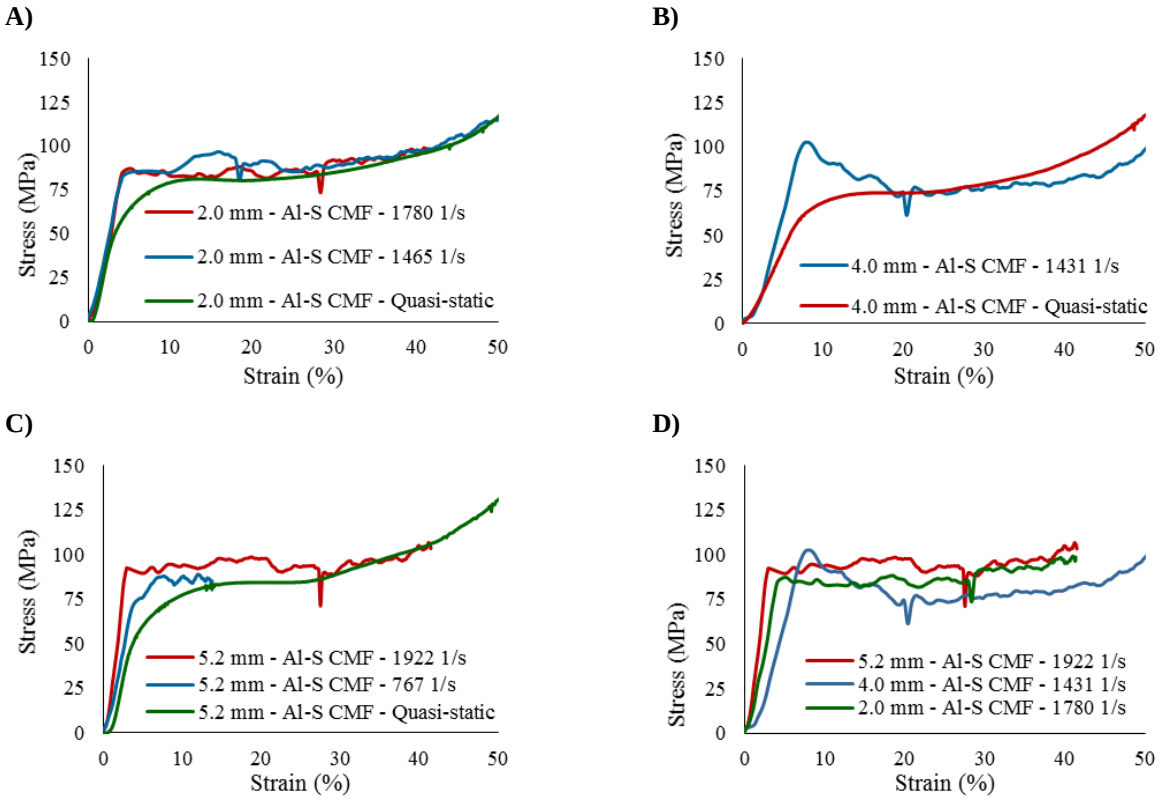


**FIGURE 23** Comparison of high-speed and quasi-static test results for Al-S CMF samples at different loading rates: A) Samples with 2 mm spheres; B) Samples with 4 mm spheres; C) Samples with 5.2 mm spheres; D) comparison of results for samples with 2 and 4 mm spheres.

Comparison of the results for cylindrical and hollow samples is shown in Figures 24a for the S-S and 24b for Al-S CMFs. It is clearly evident that quasi-static curves for both cylindrical and hollow samples are very similar. In addition, almost similar strain rate sensitivity is seen in both cylindrical and hollow samples under dynamic loading. This indicates that the quasi-static and dynamic performance of CMF is not affected by the sample's shape, while previous results presented in the project team's lower-speed dynamic testing section indicated that the CMF's performance is not affected by the sample size either.

The amount of energy absorbed during the deformation of each sample is proportional to the area under their stress–strain curves. Therefore, the high strain rate sensitivity of CMFs translates into the enhancement in their energy absorption capability. This can be observed in Tables 12 and 13 where the calculated results for specific energy absorption (energy absorption per density) of S-S and Al-S CMF samples are tabulated. Please note that different sections in this table represent the energy absorption improvement up to different strain levels (50% or 10%). As can be seen the improvement up to 10% strain is more dramatic compared to those at higher strain levels. This can be explained by evaluating the parameters contributing to the strain rate sensitivity of metallic foams. These parameters include air trapped

inside porosities, shock wave propagation, strain rate dependency of the parent metals, and micro-inertia effects.

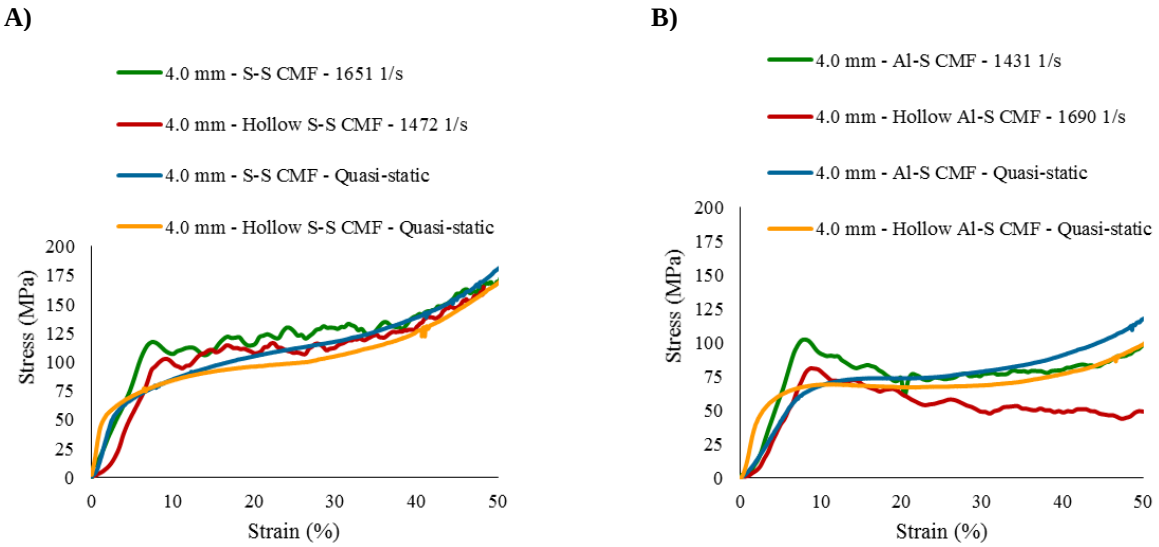


**FIGURE 24** Comparison of stress–strain results for high-speed loading a) S-S CMF and b) Al-S CMF samples with and without center hole.

Figure 25 shows the cross section of CMF samples made with 4 mm spheres using the PM technique after quasi-static and dynamic loading. As can be seen, the main feature in samples that experienced quasi-static loading is the air channels inside the matrix, which were created during the slow deformation of the sample to release the air trapped inside the spheres. For the samples that experienced high-speed loading, the bursting of spheres is the main feature. In those cases, the speed of dynamic loading does not allow the slow release of air through the matrix porosities and, instead, the trapped air will burst the shell of the spheres to release their internal pressure in a short interval during high-speed impact. Such behavior causes the additional strength of CMFs made with larger spheres under high-speed loading. Since the air trapped inside the spheres can have a more prominent effect in larger spheres, one can see a major improvement in strain-rate sensitivity of CMFs made with 5.2 mm spheres compared to those made with 2 mm spheres.

TABLE 12 Energy absorption per unit volume of S-S CMF samples at different loading rates

| 2.0 mm Sphere S-S CMF–Energy Absorption @ 50% Strain | | | 4.0 mm Sphere S-S CMF–Energy Absorption @ 50% Strain | | | 5.2 mm Sphere S-S CMF–Energy Absorption @ 10% Strain | | |
|---|---|---|---|---|---|---|---|---|
| Strain Rate ($s^{-1}$) | Energy Absorption ($MJ/m^3$) | Energy Absorption Improvement (%) | Strain Rate ($s^{-1}$) | Energy Absorption ($MJ/m^3$) | Energy Absorption Improvement (%) | Strain Rate ($s^{-1}$) | Energy Absorption ($MJ/m^3$) | Energy Absorption Improvement (%) |
| 3728 | 76.03 | 33.15 | 2740 | 67.07 | 21.46 | 1105 | 10.62 | 84.70 |
| 2629 | 72.2 | 26.44 | 1982 | 60.56 | 9.67 | 946 | 8.76 | 52.35 |
| 1523 | 62.08 | 8.720 | 1651 | 60.38 | 9.34 | 653 | 8.56 | 48.87 |
| QS | 57.101 | – | QS | 55.22 | – | QS | 5.75 | – |

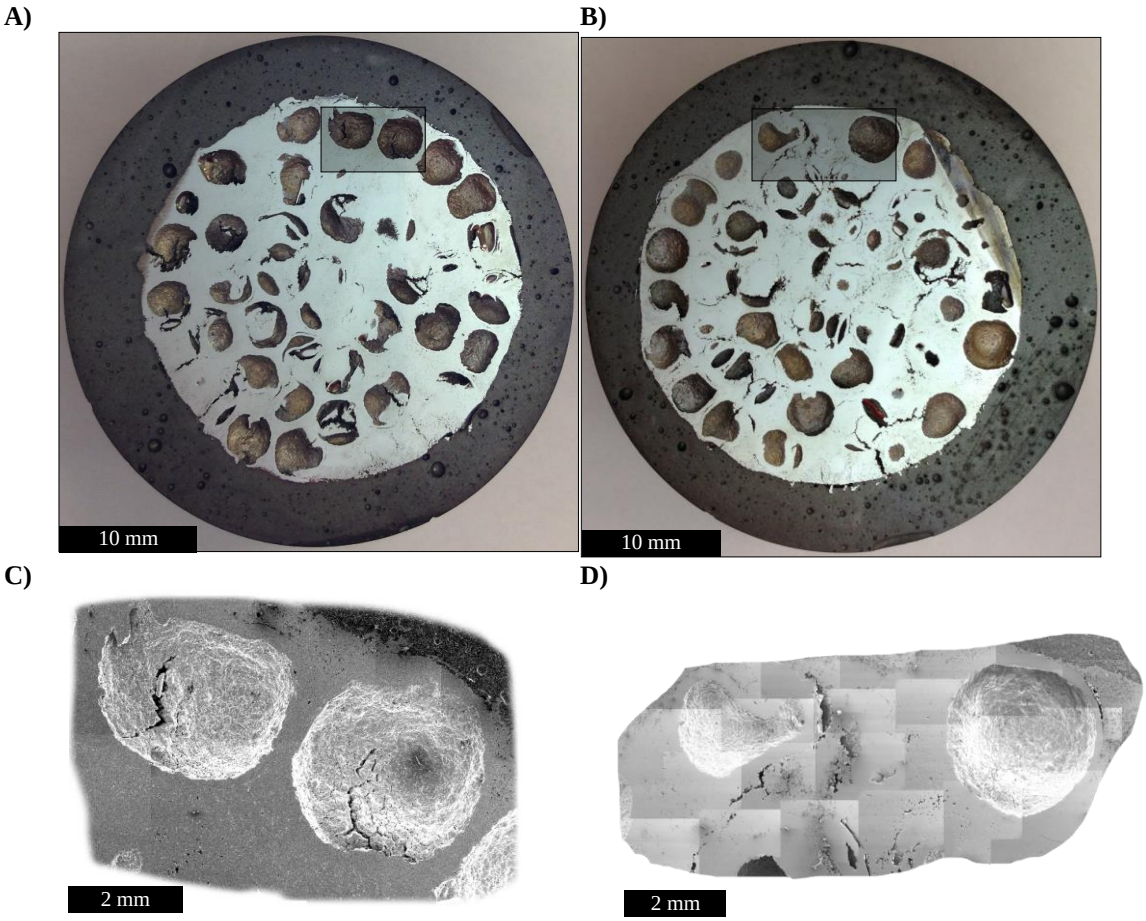


**FIGURE 25** (A and B) Optical images taken from the cross section of S-S CMF sample with 4 mm spheres after A) high-speed compression and B) Quasi-static loading. (C and D) SEM images showing the close up images of C) spheres burst due to pressurized air trapped inside them during high-speed compression and D) air channels in the matrix during quasi-static loading.

The effect of other parameters on strain rate sensitivity of CMFs was expected to be minimal. This hypothesis was evaluated and confirmed later through an extensive FEA modeling approach, in which the effect of all parameters were included except for the air trapped in the sphere walls. The stress–strain curves were generated and compared for various CMFs under different loading rates.

TABLE 13 Energy absorption per unit volume of Al-S CMF samples at different loading rates

| 2.0 mm Sphere Al-S CMF–Energy Absorption @ 50% Strain | | | 4.0 mm Sphere Al-S CMF–Energy Absorption @ 50% Strain | | | 5.2 mm Sphere Al-S CMF–Energy Absorption @ 10% Strain | | |
|---|---|---|---|---|---|---|---|---|
| Strain Rate ($s^{-1}$) | Energy Absorption ($MJ/m^3$) | Energy Absorption Improvement (%) | Strain Rate ($s^{-1}$) | Energy Absorption ($MJ/m^3$) | Energy Absorption Improvement (%) | Strain Rate ($s^{-1}$) | Energy Absorption ($MJ/m^3$) | Energy Absorption Improvement (%) |
| 1780 | 43.36 | 5.68 | | | | 1922 | 9.52 | 90.4 |
| 1465 | 43.26 | 9.36 | 1431 | 38.43 | 2.62 | 767 | 6.69 | 33.8 |
| QS | 41.03 | – | QS | 37.45 | – | QS | 5.00 | – |

## 3.2 STAGE II—NUMERICAL MODELING EVALUATION AND FINAL REPORT

### *3.2.1 Task 7: Run the modeling*

In conjunction with the experimental work reported above, a finite element analysis (FEA) model was used for simulating CMF behavior under both quasi-static and dynamic loading. To this end, ABAQUS finite element commercial codes were used to simulate the behavior of CMF under various loading rates. The finite element mesh shown in Figure 26 has a dimension of 35.33 × 35.33 × 35.33 $mm^3$ and consists of explicit eight nodal linear tetrahedral elements. The diameter of the porosities is 5 mm (similar to the diameter of spheres in CMFs) and they have an arrangement of a body-centered cubic. The actual arrangement of spheres in CMFs has a 60% packing factor and is between body centered cubic (with 68% packing factor) and simple cubic (with 52% packing factor). Therefore, a body-centered cubic packing of spheres was selected with a small gap between spheres to represent the sphere wall thickness. The presence of the gap between spheres reduces the packing factor from its maximum value of 68% to what one has in CMF (60%).

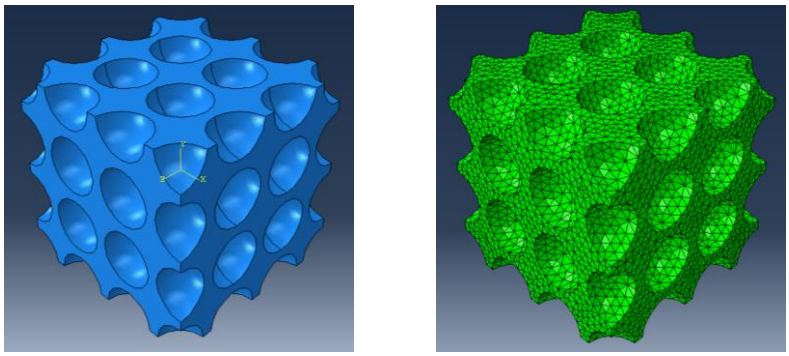

**FIGURE 26** Finite element mesh used in ABAQUS Explicit Dynamic code.

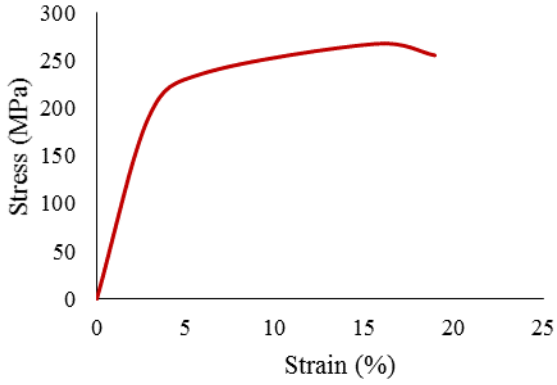


**FIGURE 27** Stress–strain behavior of A356 Al alloy used in finite element simulation.

Due to symmetry, only one eighth of the sample was modeled. A unidirectional compressive load causing 60% strain was applied on one face of the model, while the opposite face is fixed. The material difference between the sphere wall and the matrix is neglected and spheres are assumed to be fully bonded to the matrix. Linear elastic with multi-linear kinematic hardening plasticity rule and Von Mises criteria were assumed for the matrix material model based on the stress–strain data of A356 Al alloy (see Figure 27).

The strain rate sensitivity term in the Johnson Cook model was used to account for rate dependency of the aluminum alloy. This model, developed by Gordon Johnson and William Cook, is a constitutive model for ductile materials subject to high strain rates (*16*). Their material model gives an expression of stress as a function of strain, strain rate, and temperature and has become the standard when modeling metals at high strain rates. Equation 5 shows the expression of the Johnson-Cook material model, with σ being the stress, ε and $\dot{\varepsilon}^*$ the strain and reference strain rate respectively, *T** the homologous temperature, and five material constants *A*, *B*, *C*, *n*, and *m*.

$$\sigma = [A + B\varepsilon^n][1 + C ln\dot{\varepsilon}^*][1 - T^{*\,m}] \quad (5)$$

Constant *A* represents the yield strength, while constants *B* and *n* represent the strain-hardening effect. These constants can be obtained from quasi-static experimental results. In this finite element model, since the composite foams include 40% of matrix material and only 16% of sphere material with the rest being air trapped inside spheres, the dominating parameters are those related to the matrix material's properties. As a result, for aluminum–steel composite foams the properties of aluminum were used and for steel–steel composite foams, the properties of steel were used. As an example, the strain data shown in Figure 27 was used for aluminum–steel composite foams. It is notable that the sphere walls were also considered to be the same material as the matrix for simplicity. Constants *C* and ε* are the strain rate sensitivity factors of the material and are found from high-speed testing experiments. *T** gives a material softening effect with increasing temperature during high-speed loading and can be neglected as the project team's experimental work showed minimal heat generated during the high-speed impact. Such a small

amount of heat cannot have any considerable softening effect on the material. The parameters used in the project team's model are displayed in Table 14 (*17*). A modulus of elasticity of 65.12 GPa, a Poisson's ratio of 0.33, and a density of 2670 kg/m3 were assumed for the A356 Al alloy.

TABLE 14 Johnson Cook parameters used for modeling the material behavior (*17*)

| C | ε* |
|---|---|
| 0.018 | 0.7469 1/s |

Figure 28 shows the development of the normal stress in the CMF sample during high-speed compression at different strain levels. The loading speed was 120 m/s.

Results obtained from the finite element simulation were compared with experimental results in Figure 30 for both quasi-static and high-speed loading (strain rate around 1780 1/s). It can be seen that there is a good agreement between the finite element simulation and experimental results. The minor discrepancy observed at higher strain levels of dynamic loading is partly due to the difference in the strain hardening parameters between the project team's finite element model and the experiments. Another main reason for such discrepancy is related to the resistance of air trapped inside the spheres, which is not considered in this finite element model and is a subject of the project team's future studies.

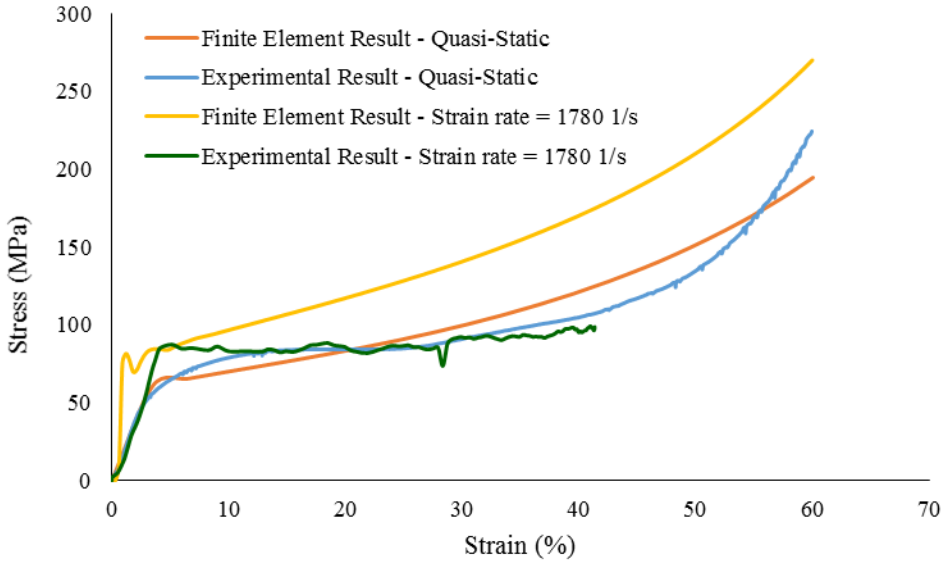


**FIGURE 28** Comparison of the results obtained from the finite element simulation and experiments for quasi-static and high-speed loading.

The deformation of CMFs under a high-speed loading rate of 1500 1/s is presented in Figure 29. As apparent in this figure, high-speed loading results in uniform deformation of spheres similar to quasi-static loading. Such behavior was also observed in images captured by the high-speed camera during the deformation of CMF under dynamic loading (Figure 21).

The stress–strain plots of CMF subjected to a variety of loading rates are depicted in Figure 30. The quasi-static data are also plotted for comparison purposes. As can be seen, the yield and plateau

strength of CMF at higher loading rates are higher than those at quasi-static loading. Parameters that are contributing to the strain rate sensitivity of metallic foams include air trapped inside porosities, shock wave propagation, strain rate dependency of the parent metals and micro-inertia effects. In the project team's finite element model all of those parameters except the effect of air trapped inside the spheres were considered. All of those parameters seemed to have minor effects on the high strain rate behavior of CMF. For instance, in Figure 31, where the effect of parent metal rate sensitivity and micro inertia is depicted, a negligible difference was observed between the data for CMF made from rate-dependent metal and that for CMF made from rate independent metal. A similar trend was also observed for micro inertia effects. Hence, it can be concluded that among the parameters contributing to strain rate sensitivity of CMF, the air trapped inside spheres has the most dominant role. As mentioned before, due to the complexity of the system, this finite element model did not account for the effect of air trapped inside the spheres. This can be the main reason between the small deviations between the project team's predicted model and experimental results for the behavior of CMFs under dynamic loading.

-

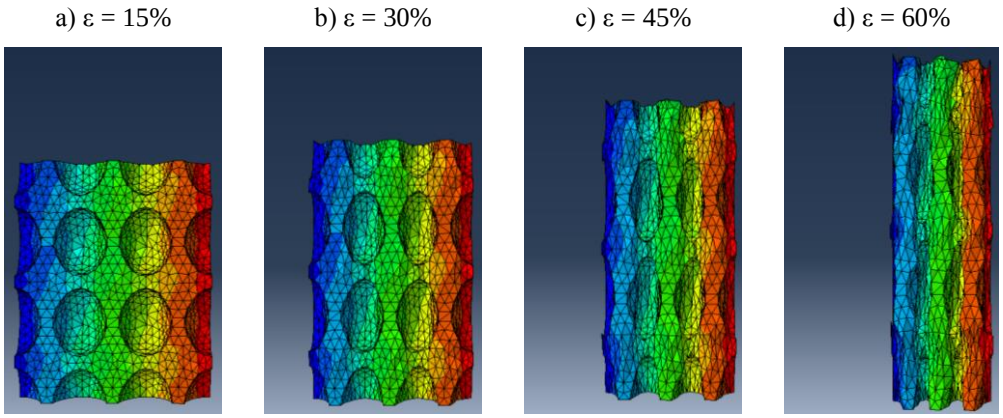


**FIGURE 29** Deformation of the finite element model under loading rate of 1500 1/s.

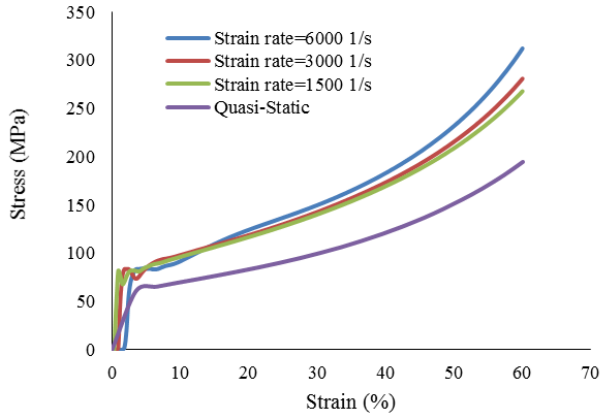


**FIGURE 30** Comparison of the results obtained from the finite element simulation for variety of loading rates.

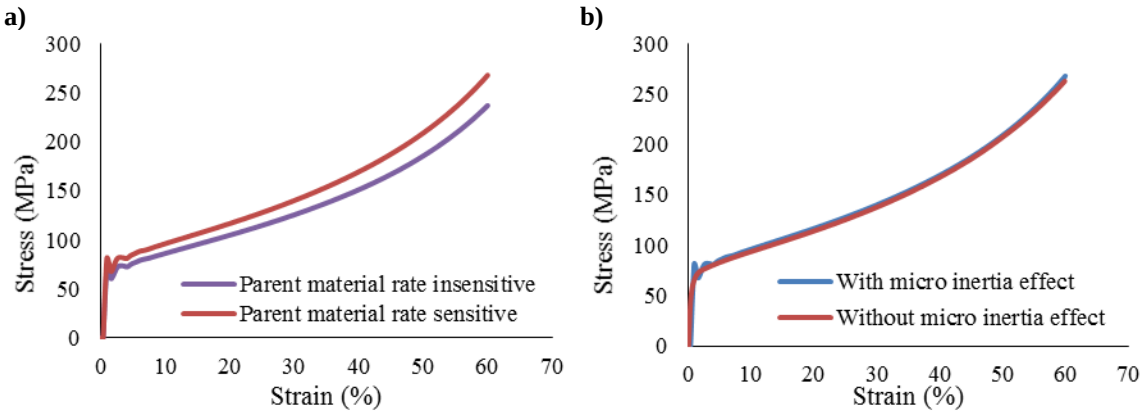


**FIGURE 31** Comparison of the results obtained from the finite element simulation for CMFs a) rate dependency effect of the parent metal; b) micro inertia effect.

### *3.2.2 Task 8: Evaluation of the efficiency*

Tables 15 and 16 show the efficiency of primary impact energy absorbers made with CMFs in comparison to the current standard crash energy management systems (CEMS) defined by FRA. In Table 15 the standard impact absorber is replaced with a cubic structure of CMF to absorb the same amount of energy defined in the standards for CEMS (2.7MJ). The efficiency is evaluated based on the weight saving and occupied space. The calculations are based on the results from both quasi-static and high-speed tests. It is clearly seen that using CMF contributes to a good amount of weight and volume savings. Moreover, the increase in energy absorption capabilities at higher speeds indicates even better efficiency.

TABLE 15 Volume saving and weight saving associated with the use of cube shape CMF with current standard CEMS (to absorb 2.7 MJ energy), "a" is the width of cube and "l" is its height. It is assumed that l/a = 3/2

| CMF | *a* (m) | *l* (m) | Volume ($m^3$) | Weight (kg) | Volume saving (%) | Weight Saving (%) |
|---|---|---|---|---|---|---|
| CMF Processed Through PM | 0.179 | 0.268 | 0.00854 | 97 | 64 | 18.0 |
| CMF Processed Through Casting | 0.207 | 0.311 | 0.01335 | 103 | 43 | 12.5 |
| PM CMF/strain rate: 2629.36 1/s | 0.176 | 0.264 | 0.00824 | 92 | 65 | 22.0 |
| PM CMF/strain rate: 3727.64 1/s | 0.168 | 0.252 | 0.00712 | 82 | 70 | 30.0 |

TABLE 16 Comparison of the energy absorption and mass of cube shape CMFs with the same volume ($10\times10\times14.4$ in$^3$) of the current standard CEMS (i.e., having 118 kg mass and 2.7 MJ of energy absorption capability)

| CMF | Energy absorption (MJ) | Energy absorption efficiency compared to current CEMS (%) | Weight (kg) |
|---|---|---|---|
| CMF processed through PM | 7.46 | 276 | 267 |
| CMF processed through Casting | 4.77 | 177 | 183 |
| PM CMF/strain rate: 2629.36 1/s | 7.73 | 286 | 264 |
| PM CMF/strain rate: 3727.64 1/s | 8.95 | 331 | 273 |

In Table 16 the energy absorption capability of the current standard CEMS is compared with a system in which the energy absorber unit is replaced with the same volume of CMF in a cubical shape of $10 \times 10 \times 14.4$ in$^3$. It can be seen that the implementation of CMFs in the structure of CEMS can provide three to four times higher energy absorption capability. The table also reveals that by increasing the loading rate, the energy absorption capacity will be increased.

To better explain the results of this study and make them comparable with the current FRA regulations and requirements for crush loads, force absorption by a 100 in$^2$ cross section of CMFs is shown in Table 17. It is notable that the cross section of the current standard Crash Energy Management System CEMS is 100 in$^2$ ($10 \times 10$). As can be seen, the maximum force absorption by either type of CMF (Al-S or SS with various sphere sizes) well exceeds the current FRA regulations of 800 kips buff strength for the under-frames of conventional equipment and 1200 kips for alternatively designed equipment.

TABLE 17 Force that can be absorbed by a 100 in$^2$ cross section of CMF at various loading rates

| **S-S CMF with spheres diameter of:** | | | | | | | | |
|---|---|---|---|---|---|---|---|---|
| | Quasi-static Loading | | | | High-speed Loading | | | |
| | 2 mm | 4 mm | 5.2 mm | 2 mm Hollow samples | 2 mm @ 3277 1/s | 4 mm @ 2740 1/s | 5.2 mm @ 1105 1/s | 2 mm Hollow samples @ 1471 1/s |
| Force Absorbed at Yield (kips) | 616 | 809.7 | 749.4 | 893.4 | 791.1 | 899.2 | 957.2 | 1842 |
| Maximum Force Absorbed (kips) | 2084 | 2011.7 | 1769.2 | 884.7 | 2675.8 | 2091.9 | 2305.8 | 2001.5 |

| **Al-S CMF with spheres diameter of:** | | | | | | | | |
|---|---|---|---|---|---|---|---|---|
| | Quasi-static Loading | | | | High-speed Loading | | | |
| | 2 mm | 4 mm | 5.2 mm | 2 mm Hollow samples | 2 mm @ 1780 1/s | 4 mm @ 1431 1/s | 5.2 mm @ 1922 1/s | 2 mm Hollow samples @ 1690 1/s |
| Force Absorbed at Yield (kips) | 826.7 | 466.4 | 797.7 | 754.1 | 933.6 | 739.6 | 1334.3 | 623.7 |
| Maximum Force Absorbed (kips) | 1377 | 1326.1 | 153.6 | 1120.1 | 1401.8 | 1479.4 | 1428 | 1174.8 |

# 4 CONCLUSIONS

The results of this study indicated a high strain rate sensitivity for both steel–steel composite metal foams (CMF) (processed through powder metallurgy) and aluminum–steel CMF (processed through casting). This can be translated to a significant improvement of their energy absorption capacity at higher strain rates, similar to those found in the collision of railroad cars.

While the strain rate sensitivity of the parent material, micro-inertia effects and shock wave propagation may contribute to the strain hardening of the material to some extent, the kinetics of entrapped air inside the spheres seems to be the main factor controlling the strain rate sensitivity of composite metal foams.

Although the normal configurations of Crash Energy Management Systems (CEMS) in railroad cars are in the form of hollow tubes with or without fillers, it was observed in the project team's studies that the sample size and shape had very minimal effects on the strength of composite metal foams under loading. That means all of the experimental results from the project team's small-scale samples (not contained in tubes) are valid for larger-scale products contained in tubes.

According to the results of this study, using steel–steel or aluminum–steel composite foams in the structure of the CEMS of railroad cars will result in a great improvement in their performance while maintaining the same weight or volume. Alternatively, using CMFs and maintaining the same performance will result in significant volume and weight savings. The maximum force absorption by either type of CMF (Al-S or SS with various sphere sizes) well exceeds the current FRA requirements of 800 kips buff strength for the under-frames of conventional cars and 1200 kips for alternatively designed cars. This can be translated into a more efficient CEMS when CMFs are implemented.

Now that the properties of the material at various high- and medium-speed impacts are established in this current project, the application of the material in an optimized design structure of CEMS is necessary in order to take full advantage of the capabilities of the material in railroad car structures.

It would seem to make sense to continue this research, including design optimization, manufacturing a full-scale CEMS prototype, and testing at a facility such as the Transportation Technology Center, Inc. (TTCI) prior to the utilization of this novel material in railroad cars. For this purpose the project team is in touch with TTCI, the Volpe National Transportation System Center and the Federal Railroad Administration to continue this effort towards manufacturing and testing a full-scale CEMS prototype and final commercialization.

# 5 INVESTIGATOR PROFILE

Afsaneh Rabiei, the PI, is a professor in the Department of Mechanical and Aerospace Engineering at North Carolina State University. Her fields of expertise include materials processing and characterization, failure- and microstructural- analysis of various traditional and advanced materials including coatings,

composites, and metallic foams. She has over two decades of experience on processing, characterization and failure analysis of metallic and composite materials and has published 6 books, one book chapter, and a number of archival articles in world-class journals.

## 6 LIST OF PUBLICATIONS

1. Alvandi-Tabrizi, Y. and A. Rabiei, "Use of Composite Metal Foam for Improving Absorption of Collision Forces," presented in MetFoam 2013, Raleigh, NC, in press by Elsevier Procedia-Materials Science 2014.
2. Alvandi-Tabrizi, Y. and A. Rabiei, "High Strain Rate Behavior of Composite Metal Foams," *Journal of the Mechanics and Physics of Solids*, in process for submission.
3. Alvandi-Tabrizi, Y. and A. Rabiei, "Finite Element Modeling of Composite Metal Foams Subjected to Variety of Loading Rates," in process for preparation and submission.

## 7 REFERENCES


1. *High-Speed Rail in America*, America 2050, Regional Plan Association, New York, N.Y., Jan. 2011.
2. National Rail Plan, Federal Railroad Administration, Washington, D.C., 2010.
3. Ashby, M.F., *Metal Foams: A Design Guide*, Butterworth-Heinemann, 2000.
4. Rabiei, A. and L.J. Vendra, "A Comparison of Composite Metal Foam's Properties and Other Comparable Metal Foams," *Materials Letters*, Vol. 63, No. 5, Feb. 2009, pp. 533–536.
5. Nevill, B.P. and A. Rabiei, "Composite Metal Foams Processed Through Powder Metallurgy," *Materials & Design*, Vol. 29, No. 2, 2008, pp. 388–396.
6. Vendra, L.J. and A. Rabiei, "A Study on Aluminum–Steel Composite Metal Foam Processed by Casting," *Materials Science and Engineering: A*, Vol. 465, No. 1, Sep. 2007, pp. 59–67.
7. Vendra, L.J., J.A. Brown and A. Rabiei, "Effect of Processing Parameters on the Microstructure and Mechanical Properties of Al–Steel Composite Foam," *Journal of Materials Science*, Vol. 46, No. 13, July 2011, pp. 4574–4581.
8. Brown, J.A., L.J. Vendra, and A. Rabiei, "Bending Properties of Al-Steel and Steel-Steel Composite Metal Foams," *Metallurgical and Materials Transactions A*, Vol. 41, No. 11, Nov. 2010, pp. 2784–2793.
9. Vendra, L.J. and A. Rabiei, "Evaluation of Modulus of Elasticity of Composite Metal Foams by Experimental and Numerical Techniques," *Materials Science and Engineering: A*, Vol. 527, No. 7, Mar. 2010, pp. 1784–1790.
10. Lakshmi, V., B. Neville, and A. Rabiei, "Fatigue in Aluminum–Steel and Steel–Steel Composite Foams," *Materials Science and Engineering: A*, Vol. 517, No. 1, Aug. 2009, pp. 146–153.

11. Rabiei, A. and M. Garcia-Avila, “Effect of Various Parameters on Properties of Composite Steel Foams Under Variety of Loading Rates,” *Materials Science and Engineering: A*, Vol. 564, No. 1, Mar. 2013, pp. 539–547.
12. Mayville, R.A., K.N. Johnson, R.G. Stringfellow, and D.C. Tyrell, “The Development of a Rail Passenger Coach Car Crush Zone,” In Rail Conference, *Proceedings of the 2003 IEEE/ASME Joint*, IEEE, 2003, pp. 55–61.
13. Strang, J., R. Hynes, T. Peacock, B. Lydon, C. Woodbury, J. Stastny and D. Tyrell, “Development of Crash Energy Management Specification for Passenger Rail Equipment,” *Transportation Research Record: Journal of the Transportation Research Board No. 2006/2007*, Dec. 2007, pp. 76–83.
14. Kremer, K. and Transportation Research Board, Metal Foams for Improved Crash Energy Absorption in Passenger Equipment, No. HSR-IDEA Project 34. 2004.
15. Deshpande, V.S. and N.A. Fleck, “High Strain Rate Compressive Behavior of Aluminum Alloy Foams,” *International Journal of Impact Engineering*, Vol. 24, No.3, Mar. 2000, pp. 277–298.
16. Johnson, G.R. and W.H. Cook, “A Constitutive Model and Data for Metals Subjected to Large Strains, High Strain Rates and High Temperatures,” In *Proceedings of the 7th International Symposium on Ballistics*, Vol. 21, Apr. 1983, pp. 541–547.
17. Gupta, S., A. Abotula, and A. Shukla, “Determination of Johnson-Cook Parameters for Cast Aluminum Alloys,” *Journal of Engineering Materials and Technology*, Vol. 136, No. 3, June 2014, pp. 034502-1–034502-4.